Biofabrication



RECEIVED 2 July 2019

.

REVISED

22 August 2019

ACCEPTED FOR PUBLICATION 30 August 2019

DUDITIONED

21 October 2019

PAPER

In vitro and in vivo evaluation of 3D bioprinted small-diameter vasculature with smooth muscle and endothelium

Haitao Cui¹, Wei Zhu¹ (10), Yimin Huang²,³, Chengyu Liu⁴, Zu-Xi Yu⁴, Margaret Nowicki¹, Shida Miao¹ (10), Yilong Cheng⁵, Xuan Zhou¹, Se-Jun Lee¹, Yifu Zhou², Suna Wang², Muhammad Mohiuddin⁶, Keith Horvath² and Lijie Grace Zhang¹,7,8,9,10 (10)

- Department of Mechanical and Aerospace Engineering, The George Washington University, Washington DC 20052, United States of America
- ² Cardiothoracic Surgery Research Program, National Heart, Lung, and Blood Institute, National Institutes of Health, Bethesda, MD 20892, United States of America
- Department of Molecular Biology, Capital Medical University Affiliated with Beijing Anzhen Hospital, Beijing Institute of Heart, Lung & Blood Vessel Diseases, Beijing 100029, People's Republic of China
- ⁴ National Heart, Lung, and Blood Institute, National Institutes of Health, Bethesda, MD 20892, United States of America
- ⁵ Department of Bioengineering, University of Washington, Seattle, Washington DC 98195, United States of America
- ⁶ Cardiac Xenotransplantation Program, Department of Surgery University of Maryland, Baltimore, MD 21201, United States of America
- Departments of Electrical and Computer Engineering, The George Washington University, Washington DC 20052, United States of America
- Bepartment of Biomedical Engineering, The George Washington University, Washington DC 20052, United States of America
- 9 Department of Medicine, The George Washington University, Washington DC 20052, United States of America
- ¹⁰ Author to whom any correspondence should be addressed.

E-mail: lgzhang@gwu.edu

Keywords: 3D bioprinting, mussel-inspired, small-diameter vasculature, endothelium, smooth muscle Supplementary material for this article is available online

Abstract

The ability to fabricate perfusable, small-diameter vasculature is a foundational step toward generating human tissues/organs for clinical applications. Currently, it is highly challenging to generate vasculature integrated with smooth muscle and endothelium that replicates the complexity and functionality of natural vessels. Here, a novel method for directly printing self-standing, smalldiameter vasculature with smooth muscle and endothelium is presented through combining tailored mussel-inspired bioink and unique 'fugitive-migration' tactics, and its effectiveness and advantages over other methods (i.e. traditional alginate/calcium hydrogel, post-perfusion of endothelial cells) are demonstrated. The biologically inspired, catechol-functionalized, gelatin methacrylate (GelMA/C) undergoes rapid oxidative crosslinking in situ to form an elastic hydrogel, which can be engineered with controllable mechanical strength, high cell/tissue adhesion, and excellent bio-functionalization. The results demonstrate the bioprinted vascular construct possessed numerous favorable, biomimetic characteristics such as proper biomechanics, higher tissue affinity, vascularized tissue manufacturing ability, beneficial perfusability and permeability, excellent vasculoactivity, and in vivo autonomous connection (~2 weeks) as well as vascular remodeling (~6 weeks). The advanced achievements in creating biomimetic, functional vasculature illustrate significant potential toward generating a complicated vascularized tissue/organ for clinical transplantation.

1. Introduction

The crux of engineering tissues/organs in regenerative medicine is to maintain metabolic functions of cellularized tissue scaffolds *in vivo*. Vascular regeneration is a necessary prerequisite for the fabrication of functional tissues/organs that recapitulate the multi-

scale structural, mechanical, and physiochemical aspects of biological functions for future clinical tissue/organ implantation applications [1–5]. Large-diameter vascular grafts (diameter >5 mm) are commercially available for clinical use; the capillaries, however, only consist of endothelial cells (several micrometers to tens of micrometers thick), which can

be spontaneously vascularized through sprout angiogenesis in vivo [2, 5, 6]. On the contrary, manufacturing small-diameter vasculature, bridging large arteries/veins and capillaries, remains a huge challenge for this field [7, 8].

Many attempts to fabricate small-diameter vasculature have been made in tissue engineering [9–12], including various 3D bioprinting techniques [5, 13–17], to mimic a vascular network that can support medium flow and oxygen supplementation for cell viability, promoting improved tissue maturation and development. Although impressive successes have been achieved, these studies have only generated endothelium via colonizing endothelial cells in the perfusable channel [5, 18]; the native structure is much more complicated. Native muscular small-diameter arteries or veins have two or three distinct tunics [11, 19]. The intima, the innermost layer, is a thromboresistant confluent monolayer of endothelial cells; the media, the middle layer, is comprised of a dense population of concentrically organized smooth muscle cells with bands or fibers of elastic tissues; and the adventitia, the outermost layer, is a collagenous extracellular matrix (ECM) containing mainly fibroblasts and perivascular nerves [11, 19]. As functional vasculature, from a pathophysiological and clinical perspective, both endothelial cells and smooth muscle cells play central roles in regulating hemodynamic forces, maintaining homeostasis, and facilitating remodeling [20-22]. Endothelium-lined vessels play an important role in maintaining the vessel wall permeability barrier, regulating coagulation (thromboresistant), and controlling blood flow, while the smooth muscle layer is vital in generating contractile forces of vasoreactivity, allowing a tolerance of systemic arterial pressures, regulating hemodynamic behaviors and other physiological activities [19, 23, 24]. Without modulation of the vascular smooth muscle, the vascular geometries present at branch points, curvatures, and post-stenotic regions would increase flow pattern disturbances, leading to endothelial dysfunction and other pathophysiological consequences, such as atherosclerosis [25, 26].

Currently, generating the stratified and self-standing vessels that replicate the complexity and functionality of native vasculature, facilitating the in vivo remodeling process and connection, remains a significant challenge. Given these requirements, it is envisaged that biomaterials play an important role in successfully engineering biomimetic vasculature. It should possess several specific characteristics: rapid and precise modeling ability; structural stability for long-term implantation; proper mechanical elasticity; excellent cell viability, adhesion, and proliferation; beneficial perfusability and permeability; biodegradability; biocompatibility; as well as bioactivity.

In this study, coaxial extrusion printing of selfstanding, small-diameter vasculature with stratified

architecture was explored using tailored bioinks. The biologically inspired catechol-functionalized gelatin methacrylate (GelMA/C), was designed and synthesized to provide the spectrum of chemical (in situ controllable crosslinking), biological (bio-functionalization), and physical (interstitial flow and elastic properties) cues for vascular bioprinting. Additionally, a fugitive crosslinking slurry was cooperatively used to support and solidify the GelMA/C bioink, thereby ensuring the successful generation of the vasculature. The stratified, independent, and free-standing architecture facilitates its integration into any engineered tissue implants, compared with dependent variations [8, 27]. To fully exploit the benefits of the 3D bioprinted vasculature for tissue regeneration, a systematic investigation both in vitro and in vivo was performed, further verifying the efficiency and advanced potential for scaling up for complex tissue/organ applications.

2. Materials and methods

2.1. Materials

All chemical reagents were from Sigma-Aldrich and were used as received unless otherwise stated. All materials in the experiments involving cell culture and animal study are pre-processed using standard sterilization methods.

2.2. Synthesis of reactive gelatin methacrylate/ catechol (GelMA/C)

GelMA/C was synthesized through a two-step chemical reaction, in which gelatin (type A; 300 bloom from porcine skin) was successively reacted with methacrylic anhydride and dopamine. Briefly, 1 g Gelatin (Gel) was dissolved in 10 ml 0.01 M phosphate buffered saline (PBS) at 60 °C. Methacrylic anhydride (10 ml) was slowly added into the 10% gelatin solution while stirring, and then reacted at 60 °C for 3 h. The product was dialyzed against deionized water for 3 d. The dialyzed solution was lyophilized to obtain pure GelMA. 1 g GelMA was dissolved in 20 ml degassed mixed solvent (2 \times PBS (pH = 5.0) and dimethylformamide (DMF), v/v = 1/1) at 60 °C. 1-ethyl-3-(3-(dimethylamino)-propyl) carbodiimide (EDC) and N-hydroxysulfosuccinimide (NHS) were added to the solution with excess molar ratio (carboxyl of GelMA/ EDC/NHS = 1:5:5). After activation for 1 d, dopamine hydrochloride was added to the solution with different molar ratios to carboxyl and stirred overnight. The crude product was purified by dialysis for 3 d in deionized water (pH = 5) and was subsequently lyophilized, which finally resulted in a white or silver GelMA/C with an average yield of 85%. The graft ratio of catechol groups in samples was calculated by measuring absorbance at 280 nm using a UV-visible spectrophotometer. The quantitative measurement was performed using a dopamine standard. The GelMA/C product was characterized using Hydrogen-1 Nuclear Magnetic Resonance (¹H NMR), and its molecular weight was measured by gel permeation chromatography (GPC).

2.3. Formation of GelMA/C hydrogels and characteristics

The GelMA/C was dissolved in PBS and then adjusted to a neutral pH of approximately 7.8 using 1 M sodium hydroxide (NaOH). To form the GelMA/C hydrogel, the GelMA/C solution was mixed with a sodium periodate (NaIO₄) solution at an equal molar ratio to catechol groups. To determine the swelling properties of the hydrogels, they were incubated in Dulbecco's modified Eagle's medium (DMEM) at 37 °C. The wet weight of the hydrogel constructs was measured at several time points during incubation. The swelling ratio of the hydrogel was calculated using the following equation:

$$SR = \frac{Ws - Wi}{Wi} \times 100\%, \tag{1}$$

Ws indicates the weight of the swollen hydrogel at each time point, and Wi indicates the initial weight of the original hydrogel on day 0.

Oscillatory rheology was performed with a Discovery HR-2 rheometer (TA Instruments). The GelMA/C solution was added directly onto the plate. After mixing with the crosslinker, a brown gel plate was immediately prepared with a diameter of 20 mm and an average thickness of 0.5 mm. The strain sweep was performed from 0.01% to 20% at a constant frequency of 1 rad s⁻¹, and a frequency sweep was performed from 0.01 to 100 rad s⁻¹ at a constant strain of 1% in the linear elastic region. No pre-stress was applied to the gels for these measurements.

The adhesion strength of the hydrogel was measured by recording detachment stress of GelMA/C hydrogel from the tissue [28, 29]. Briefly, two pieces of thin muscle tissue were clamped to each side of the tensile tester. A pre-gel solution of GelMA/C (200 μ l) was placed between the tissues and then crosslinked by adding oxidant for 10 min. The cohesive sample was pulled with a crosshead speed of 1 mm min⁻¹ until detachment.

2.4. Cell culture and maintenance

Human Coronary Artery Smooth Muscle Cells (HCASMCs, ATCC, The Global Bioresource Center) were cultured in smooth muscle growth medium for cell proliferation consisting of Medium 231 supplemented with Smooth Muscle Growth Supplement (SMGS). For smooth muscle differentiation studies, the SMGS was replaced by the Smooth Muscle Differentiation Supplement. Human Umbilical Vein Endothelial Cells (HUVECs, Thermo Fisher Scientific) were cultured in endothelial growth medium (EGM)

consisting of Medium 200 and low serum growth supplement. Human bone marrow-derived mesenchymal stem cells (hMSCs, Texas A&M Health Science Center, Institute for Regenerative Medicine) were cultured in mesenchymal stem cell growth medium (MSCGM) consisting of alpha minimum essential medium, 20% fetal bovine serum (FBS), 1% L-glutamine, and 1% penicillin/streptomycin. For the following co-culture study, vascular constructs will be optimally maintained in the mixed medium with 1:1, EGM: SMC growth medium (or SMC differentiation medium), for further characterization and *in vitro* cell studies. All experiments were performed with HCASMCs, HUVECs, and hMSCs of six cell passages or less.

2.5. 3D bioprinting of cell-laden vascular constructs

Vascular constructs were created on a customized multi-material 3D bioprinter with a coaxial needle extrusion system designed and assembled in our lab. This bioprinter consists of a transparent glass platform, equipped with a LED light array on the bottom, that controls the Z-axis motion, and an X-Y tool head coupled with coaxial nozzle connecting to two separate syringes for feeding two different bioinks simultaneously. Each ink is reserved in a syringe and deposited by applying mechanical pressure. All printing configurations are controlled by the MatterControl 1.5 software package. The printing parameters, such as printing speed (0–100 mm s⁻¹) and extrusion flow rate $(0-1.0 \text{ ml s}^{-1})$, were varied in order to obtain the best printing resolution. The coaxial needle gauges were also varied to fabricate various sizes of vessel. The inner diameter (ID) can be adjusted in the range from 500 to 1500 μ m using different coaxial needles, and the wall thickness (WT) can be controlled in the range from 100 to 300 μ m. Here, tubular lattices (interconnected vascular channels) were printed at room temperature under a sterile environment with a 5 mm line distance, and stacked layer by layer to form a cylindrical structure, mimicking vascular models within living tissue. A bioink mixture containing 20 wt% GelMA/C, and HCASMCs $(1 \times 10^6 \text{ cells ml}^{-1})$ was extruded through an external needle (18 G, diameter: 840 μ m) while a crosslinking slurry containing Pluronic F127 (30 wt%), sodium periodate (NaIO₄, 23.4 nM), and HUVECs (1 \times 10⁷ cells ml⁻¹) flowed through an internal needle (22 G, diameter: 406 μ m). Upon printing, chemical gelation was achieved by diffusion of NaIO₄ from the encapsulated slurry. Next, the 3D printed vascular construct was cultured in the cell medium and was flipped every 2-4 h for up to 24 h. Most HUVECs were floated in the hollow channel for the following cell attachment. An open, self-standing blood vessel with a bilayered cell structure was formed after removing the fugitive slurry.

Photographs and videos of vascular bioprinting were acquired using a camera and processed by imaging software. Fluorescence dyes were used to improve visualization of GelMA/C ink (Fluorescein) and crosslinking slurry (Nile red). Morphology of the 3D printed vascular constructs was observed by optical microscopy (Mu800, Amscope) with a video camera. The 3D optical map images were also performed using microscopic CCD accessories. The lyophilized morphology and microporous structure of 3D printed tubular constructs were studied with a scanning electron microscope (SEM) (FEI Teneo LV FEG). All scaffolds were coated with a 10 nm thick gold layer and imaged using a 5 kV electron beam. To visually assess cell location or arrangement in 3D printed vasculature, a fluorescent-labeled cell study was conducted. Before cell printing, HCASMCs, and HUVECs were incubated with CMFDA, and CMTDX (10 μ M Molecular Probes, CellTracker™ Dye, life technologies) each for 30 min at 37 °C, respectively. After 3 d of culture, the constructs were imaged with a confocal microscope.

2.6. Cell viability and function assay

To distinguish cell viability and proliferation after bioprinting, HUVECs and HCASMCs $(1 \times 10^5 \text{ cells ml}^{-1})$ were separately printed into the different vascular constructs. A Live-Dead assay kit (BioVision) was performed to evaluate cell viability. Printed cell-laden vascular constructs were placed onto a glass substrate and then treated with calcein-AM (2 μ M) and propidium iodide $(4 \mu M)$ for 20 min. The samples were fixed in a GelMA hydrogel, and then performed a cross-sectional cut. Cross-sectioned samples were observed and imaged using a Zeiss 710 confocal microscope. Additionally, cell activity in the printed constructs was quantitatively investigated using a CCK-8 kit. After the predetermined period, the incubation medium was changed with WST-8 solution (10% v/v in medium) (Dojindo). After 4 h of incubation, the absorbance values of the supernatant solution were measured at 450 nm on a photometric plate reader (Thermo Scientific).

Immunostaining was used to assess the cellular bioactivity for both HCASMCs and HUVECs in the 3D vasculature. The printed constructs were first fixed in 10% buffered formalin for 20 min. After fixing, constructs were permeabilized in 0.1% Triton X-100 for 30 min, and then blocked using 2% bovine serum albumin (BSA) for 2 h. Primary antibodies were incubated overnight with the constructs at 4 °C, and then secondary antibodies were incubated with the constructs for 2 h. The cells' cytoskeleton was identified with double staining of F-actin (red) using Texas Red-labeled phalloidin for 30 min and nuclei (blue) using 4,6-diamidino-2-phenylindole dihydrochloride (DAPI) (Invitrogen) for 10 min. Perfused washing with PBS was required for each step. Samples were observed and imaged using a confocal microscope.

The following primary antibodies were used for staining: Rabbit monoclonal anti-alpha smooth muscle actin ($\alpha\textsc{-}SMA$) antibodies (Abcam) and goat polyclonal anti-von Willebrand factor (vWF) antibodies (Santa Cruz Biotechnology). Goat anti-rabbit IgG H&L Alexa Fluor $^{\circ}$ 488 (Abcam) and chicken antimouse IgG-TR (Santa Cruz Biotechnology) were used as secondary antibodies in current study.

2.7. 3D bioprinting of vascularized tissue model

For vascularized tissue/organ printing, the zoning fabrication was employed through a dual bioprinting manufacturing technology. Primary cell-laden matrices with designed architectures were fabricated using a stereolithography apparatus (SLA) based 3D bioprinter (the laser beam is about 190 μ m, the wavelength is about 355 nm, and intensity output of emitted UV is $\sim 20 \mu J$ at 15 kHz), while the vasculature was printed by coaxial extrusion printer as mentioned in section 2.5. In a typical experiment, a prepolymer mixture in PBS containing 10 wt% GelMA, photoinitiator (Irgacure 2959, 0.5 wt%) and mesenchymal stem cells (MSCs) was prepared as the photocurable bioink for 3D tissue matrix bioprinting. MSC-laden tissue matrix was printed by SLA bioprinter, in which the printed vasculature was embedded during the SLA bioprinting. To visually assess cell location or arrangement in 3D printed vascularized tissue, a fluorescentlabeled cell study was conducted. HCASMCs, HUVECs, and hMSCs were incubated with CMFDA, CMTDX and CMTMR (10 µM Molecular Probes, CellTracker™ Dye, life technologies) each, respectively, for 30 min at 37 °C before cell printing. After 3 d of culture, the constructs were imaged with a confocal microscope. Similar to the method above, a Live-Dead assay was also performed to evaluate MSC viability in the 3D vascularized tissue model when perfusing medium through 3D bioprinted vasculature. The medium was perfused into the channel at a flow rate of 6.0 ml min^{-1} for 24 h.

2.8. Comparative study of alginate/calcium bioink system

The combination bioinks, composed of alginate (6 mg ml⁻¹) and calcium chloride (CaCl₂, 6 mg ml⁻¹) were used to fabricate the vasculature by coaxial extrusion bioprinting. The structural stability of the vasculature construct was studied by observing the materials' erosion or degradation for 2 weeks of perfusion. Additionally, the cell adhesion and proliferation were quantitatively measured using CCK-8 kit method described in section 2.6.

2.9. Bioactive functionalization of the construct and *in vitro* hemodynamics

The angiogenic peptide sequence with chemically functional group thiolated KLTWQELYQLKYKGINH₂ was designed and prepared to mimic the VEGF protein.

Typically, a cysteine amino acid at the N-terminus of this sequence was introduced to allow its further reaction with the methacrylate group. Peptides were obtained with more than 95% purity according to the high-performance liquid chromatography (HPLC) profile provided by the manufacturer (GenScript). After mixing with the GelMA/C bioink (\approx 7.8 in PBS), VEGF peptide (50 ng ml⁻¹) was conjugated onto the material via Michael addition reaction.

To mimic the surrounding fluid present in vivo, a custom-designed flow bioreactor system was utilized for incubating 3D bioprinted vascular constructs in dynamic culture over the whole experiment period. The constructs (vasculature embedded in GelMA hydrogel) were placed in the PDMS chamber, and culture medium was perfused using a digital peristaltic pump (Masterflex, Cole-Parmer) at a certain flow rate. To choose an appropriate flow rate, the ranges from 1 to 100 ml min⁻¹ were investigated. A fluid reservoir provided the culture medium for circulation, and a port for gas exchange, 5% CO₂/95% air was also included. For the fabrication of the PDMS chamber, PDMS (Sylgard 184, Dow Corning) base was mixed with a curing agent in a 10:1 weight ratio to make PDMS precursor. After removing air bubbles via centrifugation (5000 rpm, 10 min), the perfusable chamber was fabricated by curing at 80 °C for 1 h. The convective forces provided by creep flow, as the medium flows through the vasculature, facilitate an efficient transferring of nutrients and oxygen. Static culture served as the control and was identically operated in tissue culture wells. For the burst pressure analysis, the printed vasculature was maintained in perfusion chambers with one end sealed, and the other end attached to a differential pressure gauge. The vasculature was filled passively with PBS until failure. To perform this dynamic development in the vasculature, representative mechanical parameters, specifically wall tensile stress (*T*) in the circumferential direction, were calculated using Laplace's Law [22].

$$T = \frac{Pr}{h},\tag{2}$$

where h is the thickness of the vascular wall (mm), r is the vessel radius (mm), and P is the fluid pressure.

The average shear stress (τ) applied over the cell surface cultured in constructs was calculated using Poiseuille's law in case of laminar flow [22, 30].

$$\tau = \frac{4\mu Q}{\pi r^3},\tag{3}$$

where τ is the average shear stress over the cell surface (dyn cm⁻²), μ is the viscosity of the perfusing fluid (culture medium, 8×10^{-4} Pa s at 37 °C), and Q is volumetric flow rate (ml s⁻¹).

2.10. Vascular permeability

Diffusional permeability was quantified by perfusing culture media through the channel of 3D bioprinted

vasculature [13, 31]. Texas red-labeled 70 kDa dextran (25 μ g ml $^{-1}$, Thermo Fisher Scientific) was injected at a rate of 20 μ l min $^{-1}$ for 5 min, and then 1 μ l min $^{-1}$ for 2 h. The diffusion profile was detected and recorded every 10 min using a confocal microscope. The diffusional permeability of dextran was calculated by quantifying changes of fluorescence intensity over time using the following equation [13, 31]:

$$P_d = \frac{1}{l1 - lb} \left(\frac{l2 - l1}{t} \right) \frac{d}{4},\tag{4}$$

 P_d is the diffusional permeability coefficient, l1 is the average intensity at an initial time point (t=0 min), l2 is an average intensity after a different time interval, lb is background intensity (before injecting dextran), and d is the channel diameter.

2.11. Vasoactivity and contractile matrix deposition

To quantify the nitric oxide produced by 3D printed vasculature, after 1 d and 2 weeks of perfusable culture, the samples with 5 ml medium were maintained at -20 °C. After freezing and thawing for three cycles, proteins were removed using a microcentrifuge at 10 000 rpm for 5 min. Total nitrite in each sample was assessed using a Greiss reagent assay kit (Pierce). Samples were normalized to pure medium controls. To assess the endothelium-dependent vasodilation response, 1 μ M acetylcholine (Sigma) was added to the flow chamber for performing an acetylcholine response curve. To evaluate the effect of eNOS inhibition on the vasodilation, a final concentration of 3.2 μ M L-N^G-Nitroarginine methyl ester (L-NAME, Sigma) was added to the medium for 20 min. The construct was observed by optical microscopy (Mu800, Amscope) with a video camera, and the outer diameter change was analyzed using Image J. Changes in outer diameter are expressed as percent change from the baseline outer diameter. To assess the protein deposition of smooth muscle cells, the total collagen content was measured via Sirius red method. The suspension was dried and then incubated in Sirius red solution (0.1% Sirius red in picric acid) for 1 h, and then washed in 5% acetic acid. The resulting precipitate was dissolved in 0.1 M NaOH for 30 min. The OD was measured at 550 nm and the measurements were compared to collagen standards.

2.12. Fluorescent imaging and reverse transcription polymerase chain reaction (rt-PCR) analysis

Fluorescent imaging and rt-PCR were used to investigate 3D vasculature development *in vitro* for each condition. Printed constructs were fixed with 10% formalin for 20 min, permeabilized in 0.1% Triton X-100 for 30 min and blocked in 2% BSA for 2 h. To confirm the endothelium structure, double staining of F-actin and nuclei was performed using the method above. For immunostaining, the constructs were incubated with primary antibodies at 4 °C overnight.

The following primary antibodies were used for staining: mouse monoclonal anti-platelet endothelial cell adhesion molecule-1 (PECAM-1/CD31) antibodies (Abcam) and rabbit monoclonal anti-alpha smooth muscle actin ($\alpha\text{-SMA}$) antibodies (Abcam). After incubation with primary antibodies, chicken anti-mouse IgG-TR (Santa Cruz Biotechnology) and goat anti-rabbit IgG H&L Alexa Fluor $^{\$}$ 488 (Abcam) as secondary antibodies were added and incubated for 1 h, respectively. Fluorescence images were observed using a confocal microscope.

The gene expressions of 3D bioprinted vasculature involving smooth muscle differentiation and vasculogenesis were quantitatively analyzed by rt-PCR, including vWf, CD31, myocardin, and α -SMA. After incubation for 1 and 2 weeks, the isolation of total RNA was performed on the samples using Trizol reagent. Total RNA purity and concentration were determined using a microplate reader (OD 260/280 nm within 1.8–2.0). RNA samples were reverse-transcribed to cDNA by using a Prime-Script™RT reagent Kit (TaKaRa). RT-PCR was then performed on a CFX384 Real-Time System (BIORAD) by using SYBR Premix Ex Taq[™] (TaKaRa) according to the manufacturer's protocol. The gene expression level of target genes was normalized against the housekeeping gene GAPDH. The relative gene expression level was normalized against the control samples to obtain relative gene expression fold values and calculated via the 2-delta delta cyclethreshold (2- $\Delta\Delta$ Ct) method. Primer sequences are as follows: GAPDH, forward primer 5'-GGAGC-GAGATCCCTCCAAA-3' and reverse primer 5'-GGCTCCCCCTGCAAA-3'; vWf, forward primer 5'-CACCATTCAGCTAAGAGGAGG-3' and reverse primer 5'-GCCCTGGCAGTAGTGGATA-3'; CD31, forward primer 5'-GAGTCCTGCTGACCCTTCTG-3' and reverse primer 5'-CACTCCTTCCACCAACAC-CT-3'; myocardin, forward primer 5'-CTCGGCT-TCCTTTGAACAAG-3' and reverse primer 5'-CTTCCCAGAGAATCCATCCA-3'; α-SMA, forward 5'-CTGGGGTATTGGGGGCATC-3' reverse primer 5'-CTGTTCCAGCCATCCTTCAT-3'.

In vivo biocompatibility and biodegradation evaluation. 8-week-old, female, C57BL/6 N mice were used to evaluate biocompatibility. All of the animal experiments were approved by the Institutional Animal Care and Use Committee of the National Heart, Lung, and Blood Institute. A method of random and blinding group allocation was applied to the animal experiments. Disc-shape GelMA/C hydrogels (300 μ l) were prepared, using similar printing conditions, and equilibrated overnight in PBS. Then the hydrogel constructs were surgically implanted into the subcutaneous space on the dorsal region of the mouse. At predesigned time points, post-implantation, the animals were euthanized and the implants, together with

surrounding tissue, were harvested, fixed in formalin, and processed for histological analysis. Hematoxylin and eosin (H&E) staining was performed to evaluate the *in vivo* biocompatibility of the materials. Images were also taken to observe the degradation of the implanted hydrogels.

2.13. *In vivo* implantation of 3D bioprinted vasculature

The in vivo development of the 3D bioprinted vasculature was evaluated using a xenograft model of transplantation into six-week-old female NOD-SCID IL-2 receptor gamma null (NSG) mice. All the animal experiments were approved by the Institutional Animal Care and Use Committee of the National Heart, Lung, and Blood Institute. A method of random and blinding group allocation was applied to the animal experiments. Each NSG mouse was subcutaneously implanted with the printed cell-laden vasculature, 10 mm diameter × 3 mm thickness in size. All constructs were prepared using the protocols outlined above in a sterile condition and then surgically implanted into lateral incisions on the dorsal region. At weeks 1, 2, 4 and 6 of post-implantation, animals were euthanized and the specimens, along with the adjacent tissues, were collected for further examination.

2.14. Histology and immunohistochemistry

Samples were fixed with 10% neutral buffered formalin and processed by freezing sectioning method. The sliced samples (10 μ m) were stained with H&E through visualizing cell nuclei and cytoplasm to observe cell distribution and development in the 3D printed blood vessels. Additionally, Masson's trichrome staining was used to identify muscle and collagen fibers. To characterize vascular maturation in vivo, sections were probed with specific antibodies for the immunofluorescence evaluation. Primary antibody against the endothelial cell marker, monoclonal mouse anti-human CD31 (Dako, M0823) followed by secondary antibody labeled with Rhodamine (Jackson ImmunoResearch), were used to detect the endothelial cells and the lumen formation. For smooth muscle immunofluorescence, rabbit polyclonal anti-human α -SMA was used as the primary antibody, and FITCconjugated secondary antibody (Jackson ImmunoResearch) was stained to visualize images. All the fluorescently stained sections were counterstained with Hoechst 33258. Fluorescence images were observed using a confocal microscope.

2.15. Statistical analysis

All data are presented as the mean \pm sd (standard deviation). A one-way analysis of variance (ANOVA) with Student's t-test was used to verify statistically

Biofabrication 12 (2020) 015004 H Cui et al

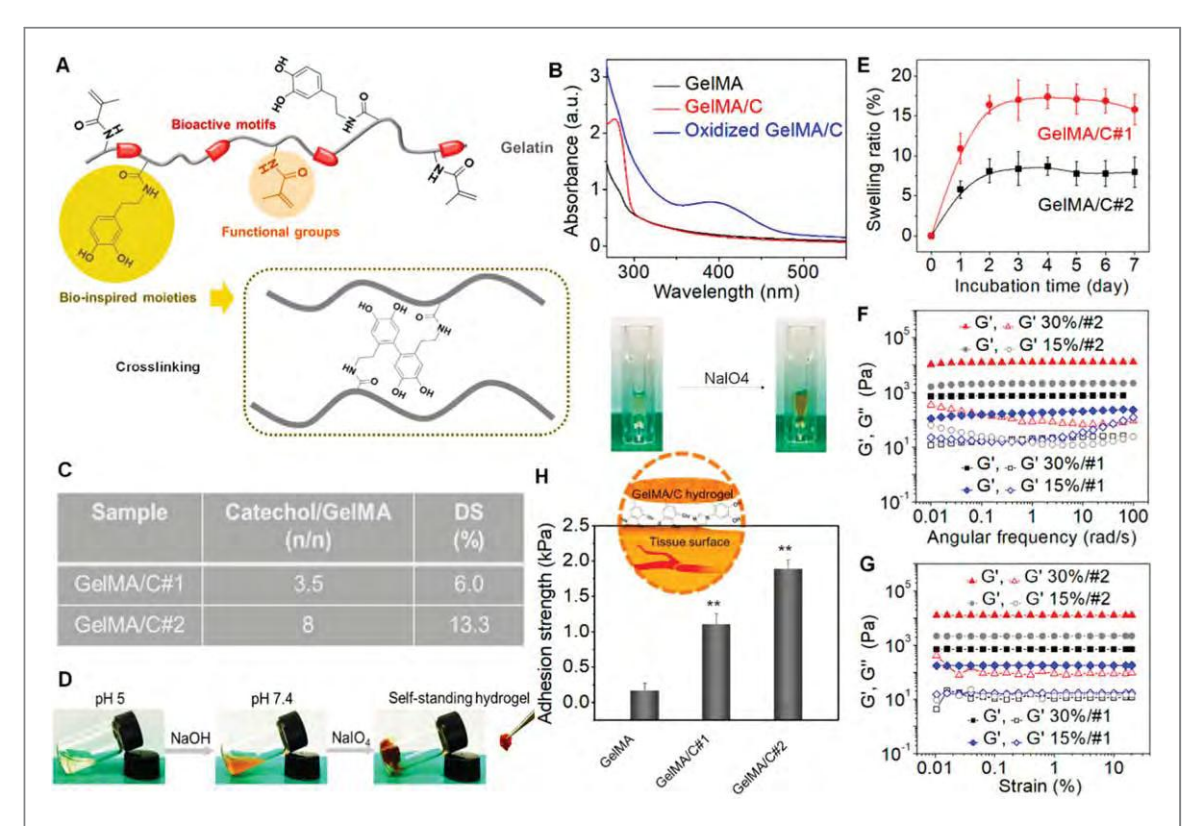


Figure 1. Characterization of GelMA/C bioink and resultant hydrogel. (A) Schematics of a GelMA/C copolymer structure and its oxidative crosslinking process, highlighting the key functional groups. (B) UV–Vis spectra of the GelMA/C solution (red line) that underwent oxidation (blue line), a GelMA solution serves as the control (black line). The colorless solution became brown after oxidation. (C) Degrees of substitution (DS) of catechol (GelMA/C#1 and #2) determined by the standard curve method. (D) Photo images of the GelMA/C gelation process. The GelMA/C solution (colorless) at pH 5 was adjusted to pH 7.8 (brown, sol), and further crosslinked to form the self-standing hydrogel (brown, gel). (E) Structural stability of the GelMA/C hydrogel in an aqueous environment through a swelling test after 7 d of incubation. (F) Dynamic mechanical analysis of the GelMA/C hydrogels. Storage moduli (G') and loss moduli (G'') evolution of the hydrogels with different DS and concentration (different colors) was measured in a frequency sweep mode. Filled symbols are storage moduli G', and open symbols are loss moduli G''. (G) Modulus-strain plots of the GelMA/C hydrogels. G' and G'' evolutions of the hydrogels with different DS and concentration was measured. (H) Adhesion properties of the GelMA/C hydrogels tested by detachment stress of hydrogel from the mouse muscle tissues. Compared with the GelMA hydrogel without catechol group, the GelMA/C hydrogels showed a significant increase in tissue adhesion ability due to a high binding affinity to peptides and proteins of the tissues; the mean \pm sd., $n \ge 9$, **P < 0.01.

significant differences among groups, with p < 0.05 being statistically significant (*, p < 0.05; **, p < 0.01; ***, p < 0.001).

3. Results and discussion

3.1. Preparation of the tailored bioink and resultant elastomeric hydrogel

A tailored bioink catechol modified gelatin methacry-late (GelMA/C, figure 1(A)) was formulated that could be crosslinked by oxidant for hydrogel formation and functionalized with bioactive factors. The GelMA/C was synthesized through a two-step chemical reaction, in which gelatin was successively reacted with methacrylic anhydride and dopamine (figure S1, supplementary figures are available online at stacks. iop.org/BF/12/015004/mmedia). Gelatin and its derivatives have been widely studied as promising biomaterials for vascular regeneration due to their native RGD (arginylglycylaspartic acid) adhesion motifs and endothelial-responsive degradation mechanism with matrix metalloprotease two or nine

[6, 13, 32]. Both play an important role in tissue remodeling associated with various physiological or pathological processes such as morphogenesis, angiogenesis, tissue repair, and metastasis, among others [33, 34]. Modification of biomaterials with a catechol moiety, known as mussel-inspired chemistry, has been widely used for surface functionalization to improve biocompatibility and enhance adhesive properties; it is also used for hydrogel formation via oxidation or enzyme induction [35-38]. In biology, dopamine, which is a typical catecholamine, plays several important roles in the nervous, immune, and digestive system as well as blood circulation [37]. In chemistry, pH-induced oxidation of the catechol group (>7.5) can result in a transition of catechol into o-quinone, which subsequently forms catechol-catechol adducts [37]. Previous studies have demonstrated that catechol modified polymers can form hydrogels in the presence of oxidants, such as tyrosinase, H₂O₂, sodium periodate (NaIO₄), and O₂ [35, 39]. Results also showed a trace amount of NaIO₄ is a preferred crosslinking agent due to its rapid gelation and high biocompatibility both in vitro and in vivo [35, 40].

According to previous studies [41], to confirm the high efficiency of carbodiimide coupling, the excessive methacrylic anhydride was reacted to ensure no active amines remained in the first step. Then bioinks with various dopamine contents were synthesized via a carbodiimide coupling reaction in (-NH₂)/GelMA (-COOH) mole ratios of 10:1 and 5:1. The methacrylate groups would further serve to immobilize the bioactive factors. ¹H NMR spectra confirmed the successful conjugation of dopamine onto GelMA by the presence of catechol proton peaks at around 7 ppm (figure S2). Figure 1(B) shows UV-vis spectra of GelMA/C and its oxidization product solutions (treated with NaIO₄). An absorption peak at 280 nm using dopamine standard solutions determined the content of catechol in the GelMA/C (figure 1(C)). After calculation, degrees of substitution (DS) of catechol was 6.0% for GelMA/C#1 and 13.3% for GelMA/C#2. GPC (water) results showed Mn (number-average molecular weight) of Gelatin was 4×10^4 with the polydispersity index (PDI) of 1.4, Mn of GelMA was 4.3×10^4 with PDI of 2.1, and Mn of GelMA/C was 4.6×10^4 with PDI of 2.3. In the current study, the gelation of the GelMA/C solution was induced by NaIO₄ with an equal molar ratio of the catechol group under neutral conditions (pH \approx 7.8) via generation of catechol-catechol adducts. Figure 1(D) shows the photo images of the hydrogel formation (15 wt% GelMA/C#2 solution shown here). The color of the solution turned brown when adjusted to neutral due to the oxidation of oxygen in the air. After adding NaIO₄ solution, the self-standing hydrogel was formed immediately. Like any other hydrogels, the gelation time of GelMA/C depended on the DS of catechol, and solution concentration (figure S3). To obtain rapid gelation for 3D bioprinting, higher than 15 wt% solution was best for the GelMA/C with a different DS of catechol after numerous trials. Additionally, when the concentration of the bioink solution was higher than 30 wt%, it became too difficult to handle for the extrusion process, largely due to its high viscosity.

3.2. Physical characterization of GelMA/C hydrogel

To study the structural stability of GelMA/C hydrogel under cell culture conditions, the swelling properties of GelMA/C hydrogel (15 wt%) in Dulbecco's modified Eagle's medium (DMEM) at 37 °C were investigated by measuring weight changes during 7 d of incubation (figure 1(E)). The swelling of hydrogels reached equilibrium or saturation in 3 d. The GelMA/C#2 hydrogels with a high DS of catechol exhibited a lower swelling capacity with more rapid saturation compared to the low DS counterparts. This is due in large part to the higher degree of crosslinking. Any significant weight change or structural deformation was never observed over the entire experiment period,

indicating the designed hydrogel would provide a stable environment for further cell loading.

Furthermore, the mechanical property of GelMA/ Chydrogel was studied, which is a key functional parameter of tissue constructs for engineered blood vessels. In addition to structural support, withstanding contractile forces within engineered constructs is also very important for regulating hemodynamic behaviors and other physiological activities. The dynamic mechanical analysis was initially performed to test the rheological properties of GelMA/C hydrogels, which are affected by DS of catechol and concentration. The storage modulus measures the stored energy of dynamic mechanical analysis, representing the elastic mechanical strength of hydrogels. As a typical characterization of sol-gel transition, convinced data can be obtained in the linear viscoelastic region by varying loading conditions, such as frequency and strain. Figure 1(F) depicts storage moduli (G') and loss moduli (G'') evolutions of hydrogels as a function of frequency. After stable gelation for 10 min, the G' for the GelMA/C hydrogel presented a substantial elastic response that was constantly greater than the G'' over the entire frequency range. As expected, a higher modulus of hydrogel would be obtained, and the modulus values changed from 10² to 10⁴ Pa when increasing concentration and DS of catechol. Additionally, all GelMA/C hydrogels exhibited a stable elastic behavior without yield or failure when varying strain from 0.01% to 20% (figure 1(G)). By modulating graft polymer compositions or solution concentration, the elastic properties of the hydrogel could be adjusted to satisfy the requirement of cellular development and biomechanics, thus improving cellular functions and offering a better hemodynamic profile. According to previous experience, the hydrogel with a higher modulus has lower cell viability due to limited proliferation space and nutrient diffusion. The elastic modulus of the printed vessel was much lower than the actual value of the native vessel, thus it is unable to directly replace the native vessels. Considering that the engineering tissue scaffolds usually serve as a temporary supporting matrix, it is expected that the ECM will be deposited to form the native tissue environment of the blood vessel with the degradation of biomaterials after in vivo implantation.

In addition to serving as the crosslinking group, the catechol can be anchored to peptides and proteins due to its high binding affinity to diverse nucleophiles (e.g. amines, thiol, and imidazole), which may enhance cell or tissue adhesion [42]. The adhesion properties of the GelMA/C hydrogels were measured by recording detachment stress of hydrogel from the mouse muscle tissues, and photocrosslinkable GelMA hydrogels without catechol groups that have similar concentration and modulus served as the control. Figure 1(H) revealed that the adhesion strength of GelMA/C hydrogels was significantly higher than that of GelMA hydrogel, and proportionally increased with

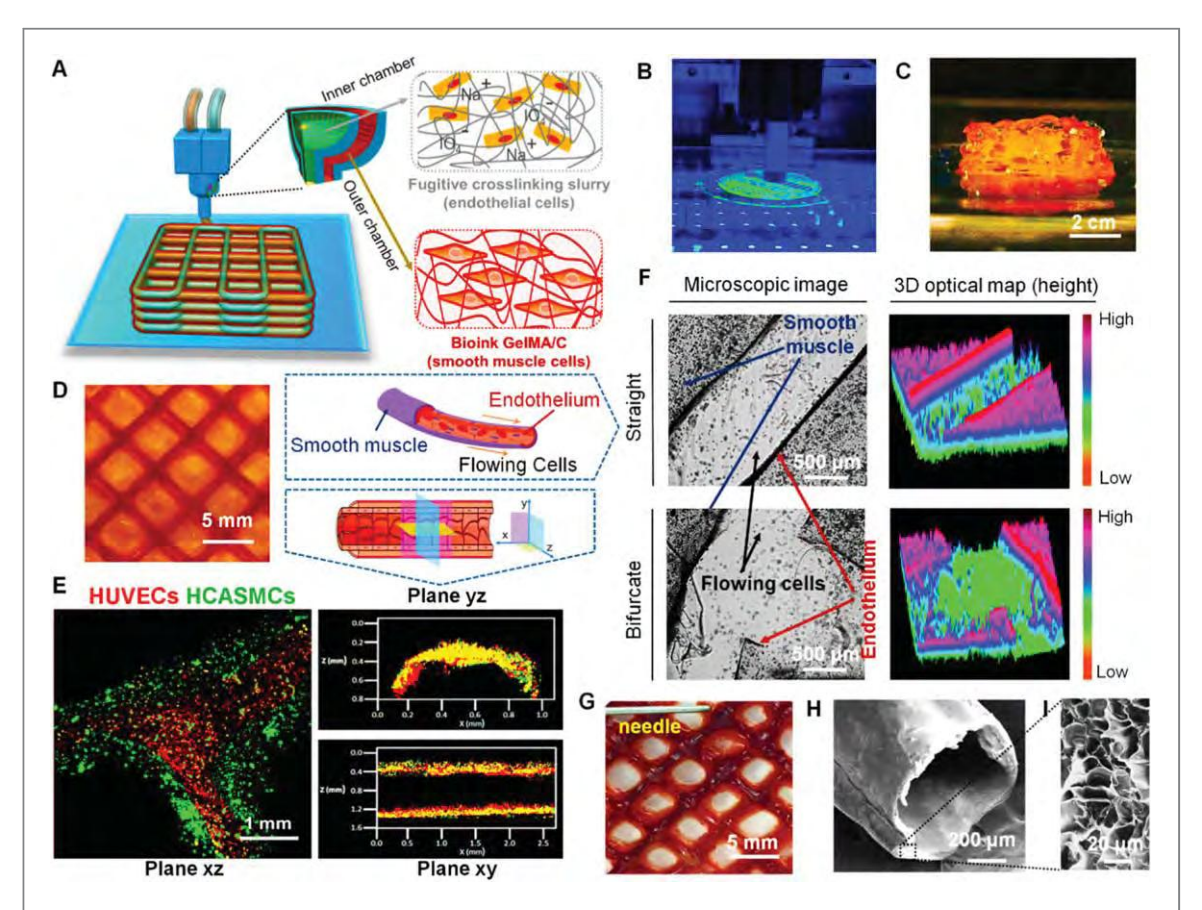


Figure 2. 3D bioprinting of vasculature construct. (A) An illustration of basic patterning of 3D vascular architecture fabricated by a coaxial extrusion bioprinter system. The 'core—shell' filament consists of two parts: (i) the inner chamber contains fugitive crosslinking slurry and endothelial cells, (ii) the outer chamber contains GelMA/C bioink and smooth muscle cells. (B) A photo image of 3D bioprinting of vasculature on the self-made bioprinter. (C) The side-view image of the 3D bioprinted self-standing vascular construct with 2 cm height. (D) The top-view image of 3D bioprinted vasculature with hollow and interconnected structure (2 layers) after 24 h of perfusion culture. (E) Structural illustration and fluorescence images of 3D bioprinted cell-laden vasculature in three different planes. Endothelial cells were colored red, while smooth muscle cells were colored green. (F) Microscopic images and their 3D optical maps (height) of 3D bioprinted vasculature (blood vessel) in straight and bifurcated regions, including smooth muscle layer and endothelium. Flowing cells were observed in the hollow channel after cell perfusion. (G) A photo image of blood plasma perfusion mimicked through a dye injection experiment. (H) Cross-sectional morphology of 3D bioprinted vasculature taken by SEM. (I) Enlarged morphology of the cross-sectional surface of 3D bioprinted vasculature taken by SEM.

increasing catechol contents. As the interaction between gel and muscle interface cannot be stronger than the inner force of hydrogel itself, the results suggested the catechol modified hydrogel possessed higher tissue adhesion compared to pure GelMA hydrogel. It is expected that the high adhesion ability would promote its integration with peripheral tissues.

3.3. 3D bioprinting of vasculature and characterization

To create self-standing vasculature with a distinct smooth muscle layer and endothelial layer in an integrated manner, a custom-designed, 3D bioprinter with a coaxial needle system was developed to directly fabricate a tubular structure, and resultant stacked networks (figure 2(A)). Nozzle size controls the vessel's ID, and printing speed and extrusion flow rate affect the vessel's WT. It is known, WT that is too thin resulted in few encapsulated cells, while WT that is too thick might induce insufficient permeation of nutrients [43]. After optimization, a small-diameter vascular construct (~1 mm tube in diameter) was

successfully produced using an 18 G external needle and a 22 G internal needle. The printing speed of the vasculature was maintained at 30 mm s⁻¹, and the extrusion flow rate of bioink for each syringe was set at 0.2 ml s⁻¹. The coaxial needle gauge can be easily replaced to achieve the fabrication of different-scale vasculature, which is similar to the reported study [43]. Although branching hierarchical trees are more biomimetic, a universal geometry-like model was chosen, which is widely used in many studies [13, 15, 44]. By replicating the essential information on structure, scale, orientation, and perfusion, it is suitable to explore a universal theory through hemodynamic experiments in the current study. Based on the material testing results above, 15 wt% GelMA/ C#2 was selected for the bioprinting and testing of vascular constructs for the rest of this study due to its high mechanical strength and low viscosity among all samples. Generally, the bioprinting step was performed by extruding bioinks through the coaxial needle (figure 2(B) and Movie S1, supplementary movies). The bioink mixture containing GelMA/C

and human coronary artery smooth muscle cells (HCASMCs) flowed through the external needle, while the crosslinking slurry containing Pluronic F127 (30 wt%), NaIO₄, and HUVECs flowed through the internal needle. Differing from the direct reaction between NaIO₄ and GelMA/C solution, the diffusion kinetics of NaIO₄ in the F127 slurry could affect the gelation process during 3D bioprinting. After numerous attempts, 5 mg ml⁻¹ NaIO₄ was successfully used in the vascular bioprinting. When the oxidant encountered the bioink, the catechol groups of GelMA/C were rapidly crosslinked to form a tube with a coreshell structure. Figure 2(C) shows a thick, vascular construct (20 layers and totally 2 cm in thickness) with regular lattice networks printed in a stackable manner, where HCASMCs were encapsulated into the shell layer, and HUVECs were encapsulated into the inner layer. As the construct was printed with a grid pattern, the supplement of nutrients and oxygen was determined by the thickness of the vessel wall. As such, it is expected that the cell viability would not be affected by the construct thickness.

The fugitive ink in the inner layer, Pluronic F127, at a certain concentration is a thermosensitive hydrogel material that is inert to cell adhesion. It can transform into a solution at low temperature or can be dissolved in water. With the fugitive slurry removal in medium, it is expected that HUVECs could migrate and adhere to the inner surface of the tube, although some of them were washed away with the fugitive removal. With 24 h of incubation in medium, a hollow, self-standing 'grid-like' vasculature construct with a bilayered cell structure was created after removing the fugitive slurry (figure 2(D)). Although the distance of each vessel was approximately 5 mm in the current images, the distance between the vessels could be optimized by changing the printing parameters, which depends on the real demand of muscularized vessels in vivo. In our preliminary trial without cells, the red dye was added to the fugitive ink to observe its removal process, thus confirming the 24 h of the postprocessing step. In other studies, a two-step method was applied to prepare the endothelium, where the F127 was rapidly removed by a cold solution flush, and then HUVECs were perfused into the lumen channel [13]. In the current design, a new method was used to ensure 'one-step' endothelium formation. In the fluorescent images, a bifurcated blood vessel sectioned from the printed vasculature was observed, which is in the form of a bilayered lumen with smooth muscle layer (green, outer layer) and endothelial layer (red, inner layer) (figure 2(E)). The cross-sectional views of a representative segment of 3D bioprinted vasculature revealed vascular lumen formation. Similar to some previous studies [13, 15], the image quality for the printed vasculature with low magnification is limited to identify cell-cell junction, but the partially enlarged scanning was conducted with high magnification in section 3.7. It should be emphasized that, rather than

traditional sacrificial template techniques, an integrative 'fugitive-migration' manufacturing approach was presented where the fugitive slurry not only provided temporary support for the tubular structures during bioprinting but also assisted in crosslinking the GelMA/C bioink for hydrogel formation. More importantly, it may also anchor endothelial cells in the channel for endothelial cell layer formation and decrease the harmful effect of the oxidative crosslinker when compared to direct permeation of oxidant solution. A different technique was developed directly to form the endothelial layer, instead of indirectly with endothelial cell perfusion, and the results were similar to, but more simple, than other endothelial cell perfusion studies [13].

After that, a cell perfusion study was performed to observe dynamic flow behavior in the 3D printed vasculature, similar to blood circulation in vivo (movie S2). Figure 2(F) shows partial view images and their 3D optical maps (height images) of straight and bifurcated structures in the vasculature construct, which suggests the vasculature is perfusable and interconnected. Notably, after cross-printing, a geometric vessel network containing well-connected bifurcated structures at each joint interface was obtained, as opposed to a broken or leaky one, which is dependent on appropriate gelation time and effective gelation fashion to ensure the fusion of hydrogel. According to the data in figure S3, a 60 s gelatin time was allowed for achieving more stable intervessel junctions of the printed vasculature. Intervessel junctions that represent a step up in complexity are the basis for native vascular architectures which terminate in a single inlet and outlet. Fluid perfusion was performed through a red dye injection experiment to confirm the interconnected feature of the vasculature for mimicking blood circulation in vivo (figure 2(G)). Additionally, the cross-sectional morphological characteristics of the 3D bioprinted vascular constructs after lyophilization were observed using a SEM (figures 2(H) and (I)). The inner structure of a porous network in the vessel wall could be beneficial to the exchange of nutrients and gases in the cell-laden construct.

To maintain the long-term function of engineered tissue, the bioprinted construct must be able to maintain cellular homeostasis, self-renewal, and development. Both printing procedure (bioink, time, and printing modality) and post-printing culture may impact the cell viability. After bioprinting, the viability and proliferation of encapsulated HCASMCs and HUVECs were evaluated in the 3D printed vasculature. After 1, 3, and 7 d of culture, the Live-Dead staining (figure S4) indicated that the cell viability of both HCASMCs and HUVECs was preserved and not significantly influenced by the bioink materials (GelMA/C) and crosslinking agents (NaIO₄ and F127). Initial death of cells was observed on the first day due to the high shear force experienced during bioprinting and hydrogel encapsulation. However, it was significantly reversed with cell proliferation over

the prolonged culture period. The results were normalized to the whole fluorescence area at day 1 (the initial cell viability was defined to 100%, so total cell viability was shown to be >100% after 7 d of culture). Moreover, cell metabolic activity (or proliferation) was investigated up to 7 d (figure S5). The results showed that both HCASMCs and HUVECs had increased metabolic activity in the 3D printed vasculature, although their activities are lower than the control groups (TCPs) due to the initial cell death and loss during vasculature fabrication. Additionally, it is likely that the reduced metabolic activities of these cells are a result of limited nutrient availability through the vascular constructs compared to the control conditions. The differences in metabolic activity between HUVECs and HCASMCs could be attributed to HUVECs being grown on the surface of the vasculature while HCASMCs were encapsulated into the vasculature hydrogel.

In previous studies, coaxial extrusion bioprinting succeeded in producing a vascular architecture with perfusable lumen [43, 45–47]. They all employed combination bioinks, composed of alginate and calcium chloride (CaCl₂), however, some reported weaknesses, such as non-cell-adhesive properties, low proliferation abilities, and instability for long-term culture potentially limiting practical application [48, 49]. To demonstrate the advantages of the tailored bioinks, the cell adhesion at 6 h and proliferation at 7 d were investigated on different materials (figure 3(A)). These time points were selected based on the adhesion, spreading, and proliferation kinetics of endothelial cells in a previous study [50, 51]. Data showed HUVECs had a significantly better adhesion after 6 h of culture, and a higher proliferation after 7 d of culture on the surface of GelMA/C hydrogels compared to alginate hydrogels. Moreover, the alginate hydrogels exhibited degraded structural stability after 2 weeks of perfusion (figure 3(B)) [52, 53]. Therefore, it is expected that the GelMA/C vessel would have high vessel durability, ensuring blood flow stability. These results suggested the new bioink possessed excellent characteristics, such as surface endothelization and mechanical stability, on fabricated vasculature constructs.

3.4. 3D bioprinting of vasculature application: SLA-printed tissue matrix with coaxial extrusion-printed vasculature

Beyond the independent vasculature or blood vessels, the goal of bioprinting vasculature is to integrate it into engineered tissue matrices for maintaining metabolic functions. To verify this hypothesis, a dual 3D bioprinting platform was applied to generate a thick tissue matrix with embedded geometric vasculature (figure 3(C)). The uniqueness of the dual printing platform is to integrate two different bioprinting mechanisms (laser-based SLA and coaxial extrusion systems) into one [5]. As the extrusion-based

bioprinting is limited by its low resolution, the highresolution SLA printer was used to cure the gelatinbased bioink into the precisely patterned structure for tissue matrix fabrication using a similar method from our previous papers [54-56]. Human bone marrowderived mesenchymal stem cell (hMSC)-laden GelMA hydrogel, fabricated by SLA bioprinting, was used as a universal tissue matrix model. During SLA bioprinting, the 3D bioprinted vasculature was embedded into the hMSC-laden constructs (figures 3(D) and (E)). Compared to the extrusion bioprinting, the advantage of SLA bioprinting, used here, is its ability to fabricate a 3D geometrical structure with a high-resolution, although the negative effect of photocrosslinking on cell viability is a consideration. The embedded vasculature was designed to ensure uniform nutrient supplementation throughout the surrounding matrix.

In physiology, endothelium permeability in the vasculature is pivotal in the exchange of nutrients and gases with the peripheral tissue. Therefore, an effective permeability of printed vasculature is required to maintain the function of the vasculature itself and the peripheral engineered tissues. The Live-Dead cell staining was performed to investigate the hMSC viability in the hydrogel-based tissue matrices where the nutrient was provided by the adjacent vasculature (figure 3(F)). It is observed that cell viability significantly reduced beyond 300 μ m from the vessel, suggesting a typical diffusive limitation. It indicates that the 3D bioprinted vasculature could provide efficient nutrient distribution through diffusing medium to hMSCs in the matrix for supporting peripheral tissue viability and development.

3.5. Bioactive functionalization and *in vitro* hemodynamic study

In addition to maintaining cellular bioactivity, it is crucial to provide an adequate bio-microenvironment including mechanical, chemical or biological signals for regulating engineered tissue remodeling and maturation. The biofunctionalization, involving the incorporation of bioactive factors, enzymatic recognition sites, and adhesion factors among others, is a promising approach for directly activating cellular signal pathways during tissue development. In this study, the methacrylate groups in the tailored bioink can be chemically immobilized with bioactive factors as in a previously reported study [57]. Thiol-functional oligopeptides with sequences of KLTWQELYQLKYKGINH2 derived from the knuckle epitopes of vascular endothelial growth factor (VEGF) were conjugated to the GelMA/C polymer (figures 4(A) and S6), which was verified as a highly effective factor for vasculogenesis [6, 58]. Compared to directly incorporating VEGF growth factor, the peptide not only delivers specific bioactive factors in a uniform manner for guiding vascular formation, but also addresses issues of prolonged tissue retention and sustainable bioactivity compared to traditional growth factor encapsulation. As

Biofabrication 12 (2020) 015004 H Cui et al

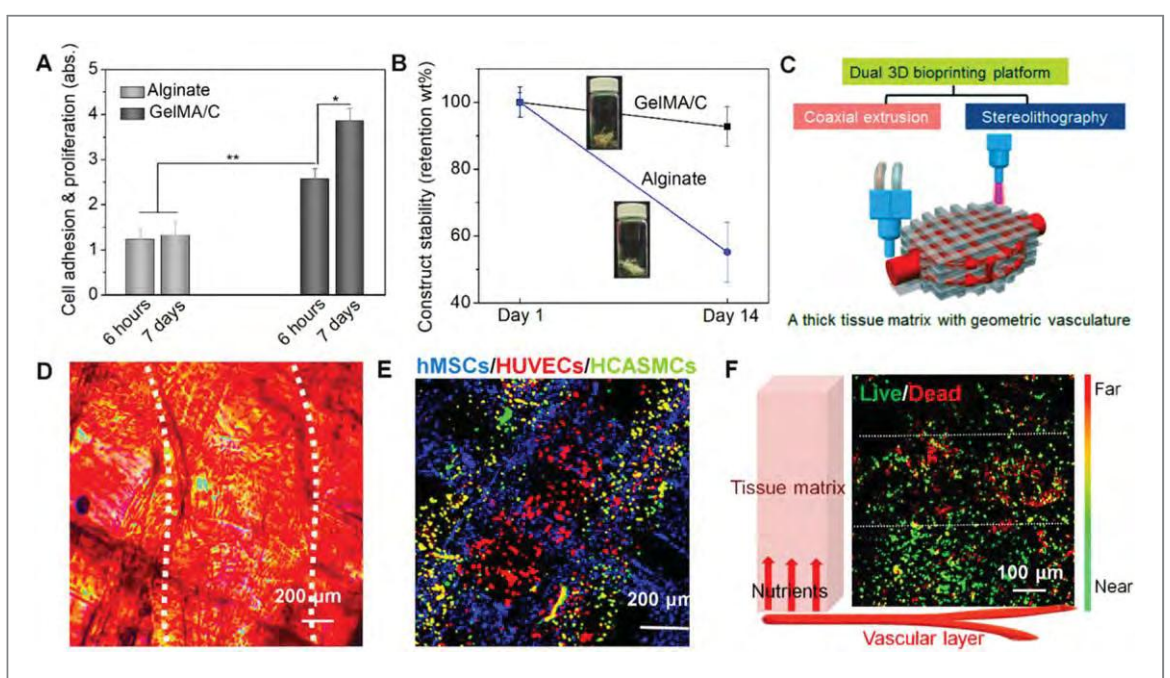


Figure 3. 3D bioprinting of alginate-based vasculature and 3D bioprinting of tissue matrix with the vasculature. (A) Cell adhesion and proliferation of vascular constructs fabricated by GelMA/C and traditional alginate; the mean \pm sd., $n \geq 9$, $^*P < 0.05$, $^{**}P < 0.01$. (B) Structural stability of vascular constructs fabricated by GelMA/C and traditional alginate. (C) Schematics of a dual 3D bioprinting platform (coaxial extrusion and stereolithography) to be applied to generate thick, vasculature embedded tissue matrix, where the vascularized tissue is fabricated with vasculature in a 'sandwich' manner. (D) Microscopic images and (E) a fluorescence image of a 3D bioprinted cellularized tissue matrix. The white dotted lines in D indicate the position of 3D printed vasculature. Dual-layered vasculature (smooth muscle, green; endothelium, red) was embedded into an MSC-laden tissue matrix (grid, blue). (F) Nutrient supplementation assay of encapsulated MSCs in the vascularized tissue using Live-Dead staining. Near/Far dedicates the distance away from the vasculature in the schematic. White dotted lines sperate into three zones, i.e. death zone without enough nutrients, transitional zone, and survival zone with enough nutrients. It showed an effective supplementation of nutrients for cell viability related to diffusion.

a small number of peptides were added, obvious spectra signals by IR and NMR were not successfully detected, where only the strong signals of the gelatin were observed [6].

Blood vessels are normally exposed to two types of mechanical forces in vivo: (a) circumferential stress acting tangentially on the vascular wall and directly related to pressure and dimensions (diameter and thickness) of the vessel, and (b) shear stress acting in the longitudinal direction at the blood-endothelium interface and directly related to the flow-velocity profile. To investigate the functional characteristics of the perfusable vasculature in a fluid dynamic environment, the vascular constructs were installed in a PDMS chamber with a single inlet and outlet, connected to a customized bioreactor. The embedded vascular network in the GelMA hydrogel constructs was designed as an asymmetrically branched structure to ensure uniform perfusion throughout the tissue for transporting nutrients, oxygen, and waste materials (figure 4(B) and movie S3). To minimize the mechanical effect of the mounted hydrogel on the vascular construct, a distinctly softer hydrogel (only 2×10^2 Pa) was used. Figure 4(C) illustrates the circumferential stress and shear stress during the perfusion culture. The flow rate with respect to the fluid pressure was varied to observe the distensibility

of the vasculature construct. Burst pressure was measured by pressurizing vasculature constructs with PBS until failure (figure 4(D)). Compared to static culture, dynamic culture increased the mechanical properties of the constructs after 7 d. Although the burst pressure result is slightly lower than the native vessel, the engineered vasculature is suitable for supplying the blood within the engineered tissue constructs when compared to other studies [8]. Considering the elasticity and stability of 3D bioprinted thin vascular walls, a flow rate of 6.0 ml min⁻¹ was selected after initial screening, for the dynamic culture studies. Through calculation, the average tensile stress (T) of the vasculature was 16.7 kPa (\sim 62.5 mmHg), and the average shear stress (τ) was approximately 8.2 dyn cm⁻², which is within the range (from 5 to 12 dyn cm⁻²) of shear stress in the microcirculation [26]. The Laplace and Poiseuille's law were applied here as typical equations to obtain the value of hydrodynamics according to previous studies [22, 30]. The vasculature constructs were perfused for 2 weeks to evaluate vessel maturation and vasoactivity over time.

3.6. Vascular permeability, vasculoactivity, and ECM deposition

Maintenance of the size-selective sieving property of endothelium is crucial for several physiological functions, including normal tissue-fluid homeostasis, Biofabrication 12 (2020) 015004 H Cui et al

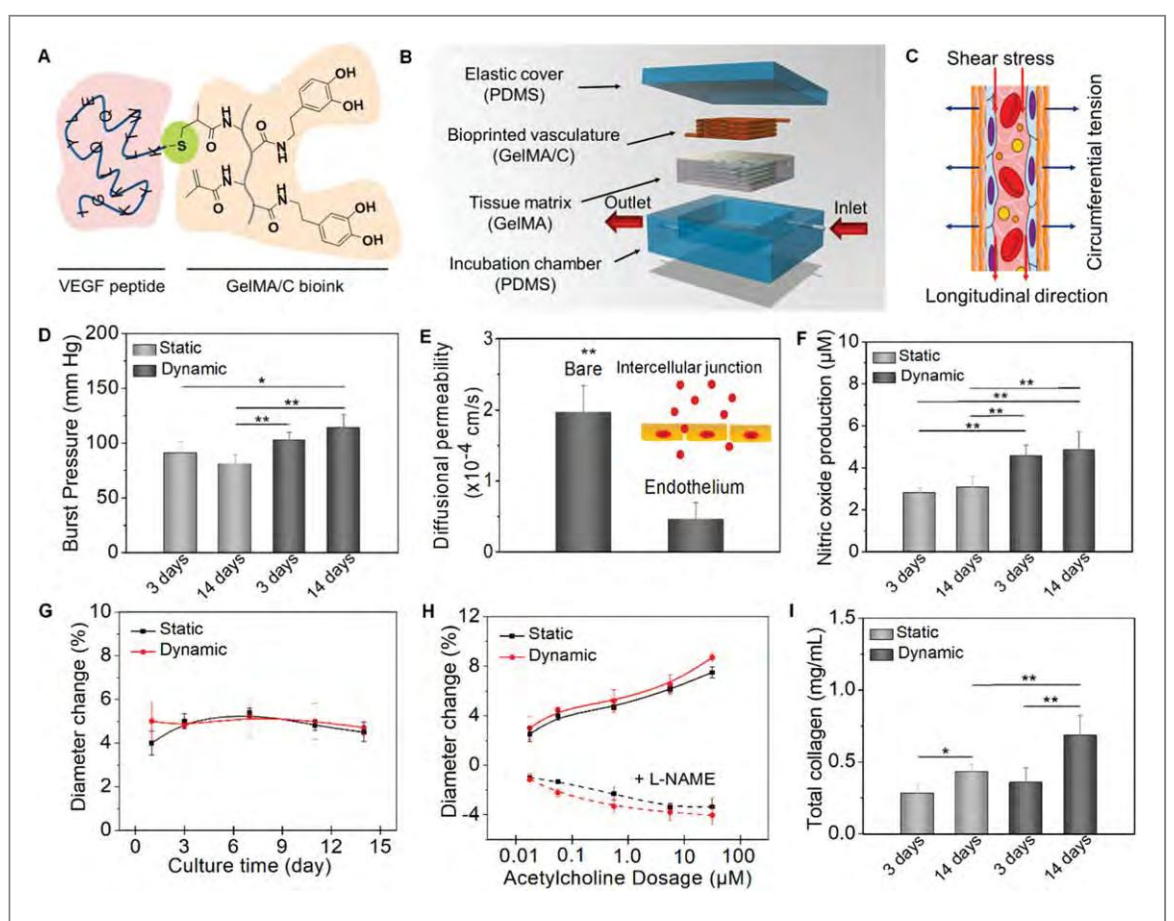


Figure 4. Hydrodynamics, vasculoactivy, and extracellular matrix deposition. (A) Schematics of chemical immobilization of VEGF peptides onto GelMA/C bioink. A Michael addition reaction between methacrylamide and thiol-functional oligopeptide was performed for ink bio-functionalization in current design. (B) An illustration of dynamic perfusion culture. The vasculature with one inlet and one outlet was embedded into a tissue matrix (GelMA hydrogel as a supporting material) and then placed into a customized PDMA chamber. (C) An illustration of the circumferential stress and shear stress during the perfusion culture. (D) The burst pressure of 3D printed vasculature constructs under static and dynamic culture; the mean \pm sd., $n \ge 9$, $^*P < 0.01$. (E) Quantification of barrier properties confirmed by the comparison of a bare channel (without endothelial lumen) and endothelial lumen. Both contain smooth muscle cells. By mimicking native endothelial functions, vascular permeability originates from the intercellular junction; the mean \pm sd., $n \ge 9$, $^*P < 0.01$. (F) Nitric oxide production of 3D printed vasculature constructs under static and dynamic culture; the mean \pm sd., $n \ge 9$, $^*P < 0.01$. (G) Vasodilation response to 1 μ M acetylcholine of 3D printed vasculature constructs under static and dynamic culture; the mean \pm sd., $n \ge 6$. (H) Dose-dependent vasodilation response to acetylcholine of 3D printed vasculature constructs and their constriction induced by pre-treat of L-NAME under static and dynamic culture; the mean \pm sd., $n \ge 6$. (I) Total collagen synthesis of 3D printed vasculature constructs under static and dynamic culture; the mean \pm sd., $n \ge 9$, $n \ge 0.01$, $n \ge 0.01$, $n \ge 0.01$.

angiogenesis, vessel tone, and host defense, which involves two endothelial transport mechanisms, transcellular and paracellular pathways [59]. To further assess the permeability function of the printed vasculature, dextran was used as a macromolecular model to test the diffusional permeability (figure 4(E)). After the endothelial layer formation in the vascular channel, the permeability of medium diffusing from the vasculature to the thick tissue matrix was observed at approximately 4.67×10^{-5} cm s⁻¹; this is consistent with convective diffusion transport and metabolic conversion within the tissue. Additionally, compared to the bare channel (without endothelial layer), a significant (almost 4.5 fold) reduction in permeability and no significant leakage of the culture medium during perfusion into the vasculature channel was observed. It can be concluded that the endothelial layer is dominating transport resistance, like the way it governs the permeability of blood vessels *in vivo*.

Physiologically relevant reactions to vasoactive stimuli were studied by nitric oxide (NO) release and endothelium-independent vasodilation for 2 weeks of culture. The endothelium synthesizes and releases NO to maintain homeostatic function; endothelium-derived NO maintains a non-thrombogenic surface, prohibits leukocyte attachment, and promotes vascular relaxation under basal conditions [60, 61]. NO produced by endothelial cells was evaluated by assessing total nitrite concentration, the stable NO metabolism byproduct under physiological conditions (figure 4(F)). NO production of the 3D printed vasculature constructs after 3 d of culture was close to the value after 2 weeks, in static culture. The dynamic culture significantly improved the NO production of the

constructs when compared to the static culture. To further explore the role of NO in the endotheliumdependent vasodilation in the vasculature constructs, the effect of vessel diameter on the responses to acetylcholine (an endothelium-dependent vasodilator) with or without L-N^G-Nitroarginine methyl ester (L-NAME, an inhibitor of endothelial nitric oxide synthesis (eNOS)), were investigated [62, 63]. After 1 μ M acetylcholine was added into the culture medium, the diameter of the vasculature constructs dilated about 5%, and maintained relative stability for vasodilation response over 2 weeks, suggesting sustained endothelial health of the 3D printed vasculature (figure 4(G)). The dose-response of acetylcholine from 0.01 to $100 \,\mu\text{M}$ showed increasing vasodilation for 2 weeks; however, after pre-treating with L-NAME for 10 min, the vasculature constructs exhibited vasoconstriction in the same conditions (figure 4(H)). The results demonstrated that the vasodilation in response to acetylcholine was attributed to the NO release of the 3D printed vasculature. Additionally, collagen is the major matrix constituent of the vessel wall and is synthesized by smooth muscle cells [64, 65]. Therefore, total collagen synthesis was used to quantify the ECM protein deposition. Figure 4(I) shows that collagen production was increased over 2 weeks of culture, and the collagen content under dynamic culture was significantly higher compared to static culture. It indicated that hydrodynamic culture or biomechanical stress could improve the ECM deposition of 3D printed vasculature constructs. In the previous study, Tranquillo et al have also verified that mechanical forces play an important role in shaping the organization of the ECM when they applied a cyclic stretch or pulsed flow stretch to the grafts in a bioreactor [66, 67].

3.7. Vasculogenesis and contractile protein expression

For the functional development of 3D bioprinted vascular constructs, smooth muscle differentiation medium was added to induce HCASMC differentiation according to Thermo Fisher's protocol (HCASMCs will undergo a cessation of growth, a change in cellular morphology from slender stellate cells to enlarged rectangular or triangular shaped cells, and will express increased amounts of smooth muscle α -actin over the course of 2–8 d). After 2 weeks of active perfusion, the structure of 3D bioprinted vasculature maintained good integrity under a shear stress of 8.2 dyn cm⁻². As shown in figure S7, these endothelial cells maintained their endothelial phenotype and distributed uniformly around the lumen characterized by expression of platelet endothelial cell adhesion molecules (PECAM-1/cluster of differentiation 31, CD31; makes up a large portion of endothelial cell intercellular junctions involved in leukocyte transmigration, angiogenesis, and integrin activation).

Moreover, smooth muscle cells encapsulated in the outer layer exhibited the α -actin phenotype of smooth muscle (α -SMA, are highly conserved proteins that are involved in cell motility, structure and integrity, and a major constituent of the contractile apparatus). However, as our vascular construct diameter (>1 mm) is larger than the resolution of confocal microscopy, it is hard to identify the confluent feature in the tile scanning model [13]. Thus, partially enlarged scanning with a high magnification was performed. In response to an integrated stimulus with angiogenic VEGF peptide and dynamic culture, Vinculin staining showed HUVEC growth was aligned with flow direction, which can be attributed to the shear stress (figures 5(A) and S8). Vinculin is a protein that couples, transmits, transduces, and regulates mechanical force between the cytoskeleton and adhesion receptors. F-actin and VE-Cadherin staining of HUVECs also revealed a confluent endothelium with intercellular junctions on the lumen surface of 3D bioprinted vasculature at day 7, and the HUVEC behaviors were similar to a previous study [13] (figures 5(B) and S8). Additionally, smooth muscle cells exhibited a switch to contractile phenotype (fusiform or elongated shape) with a strong axial alignment compared to the control, identified through costaining of F-actin and α -SMA (figures 5(C) and S8). As mentioned above, the results further demonstrated the ECM alignment or contractile protein organization was determined by the mechanical stretch direction as evidenced previously [67].

To determine cellular functions in the 3D bioprinted vasculature, relative gene expression including endothelial function and smooth muscle differentiation was quantitatively measured by RT-PCR using GAPDH as a housekeeping gene. To deconvolute the mixing effects for co-culture, a pure cell population experiment was conducted. As shown in figures 5(D) and (E), after 2 weeks of culture the von Willebrand factor (vWf, a blood glycoprotein) and CD31 expression in the VEGF peptide bonding groups showed increased vasculogenesis both in static and dynamic culture conditions. This demonstrates the ability of immobilized VEGF peptides to enhance signaling and bioactivity of endothelial cells and consequent vasculogenesis in vitro. Moreover, the vWf expression of the VEGF peptide bonding group in the dynamic culture is up-regulated 7-fold compared to the static culture. The expression of α -SMA and myocardin (Myo, a smooth muscle-specific transcriptional coactivator of serum response factor) has a similar tendency with the gene expression level of the dynamic culture group being much higher than the static culture counterpart (figures 5(F) and (G)). The results suggest that perfusion culture produces a beneficial effect for vascular smooth muscle formation by undergoing contractile force associated with hemodynamic pressure [20, 22, 68]. Additionally, it was also observed that the VEGF peptides promoted smooth muscle differentiation of HCASMCs

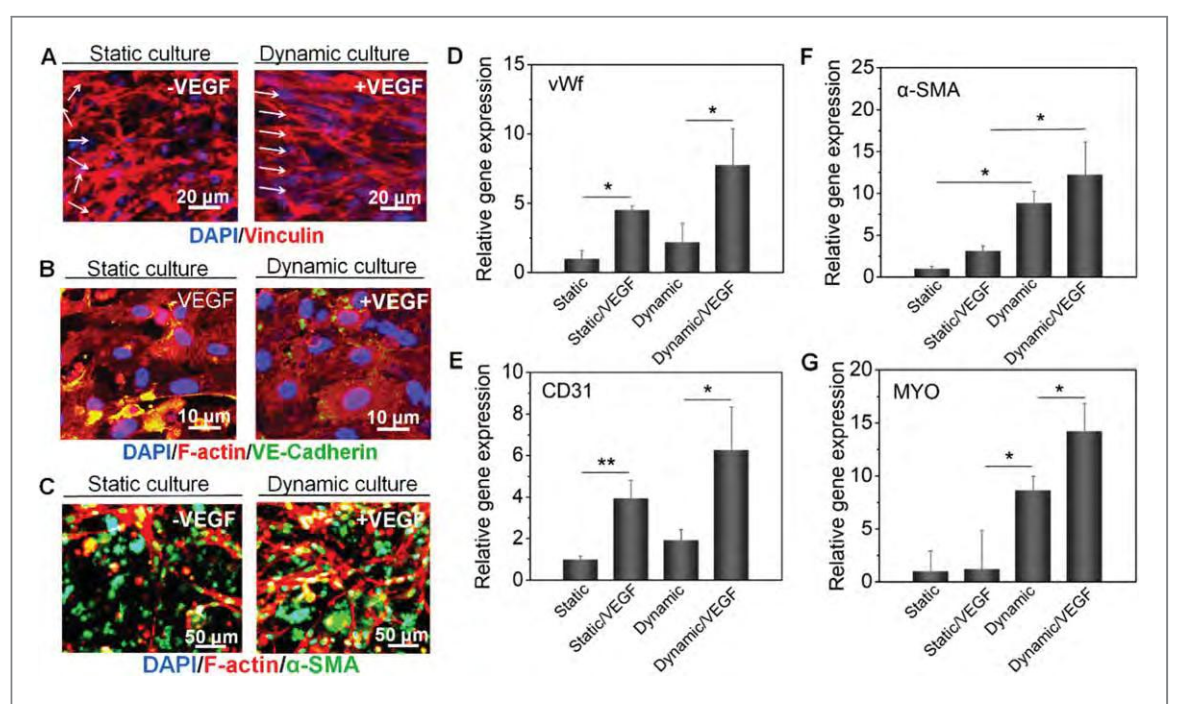


Figure 5. Vasculature development study *in vitro*. (A) Immunofluorescence images of the endothelium (spreading and orientation) of 3D bioprinted vasculatures (vinculin, red; DAPI, blue) including +VEGF/dynamic group and -VEGF/static group. Images of other groups are shown in the supplementary file. (B) Immunofluorescence images of the endothelium (intercellular junctions) of 3D bioprinted vasculatures (VE-cadherin, green; F-actin, red; DAPI, blue) including +VEGF/dynamic group and -VEGF/static group. Images of other groups are shown in the supplementary file. (C) Immunofluorescence images of the smooth muscle of 3D bioprinted vasculatures (α -SMA, green; F-actin, red; DAPI, blue) including +VEGF/dynamic group and -VEGF/static group. Images of other groups are shown in the supplementary file. (D)–(G) Relative gene expression of vWf (D), CD31 (E), α -SMA (F), and MYO (G) with univariate analysis, including +VEGF/dynamic group, -VEGF/dynamic group, +VEGF/static group, and -VEGF/static group; the mean \pm sd., $n \ge 9$, *P < 0.05, **P > 0.05, **P

to some extent. Overall, the VEGF peptides improved vasculogenesis and smooth muscle differentiation of 3D bioprinted vasculature by providing a positive biological stimulus, while perfusion culture facilitated an efficient bio-environment, through both homogenous mass transport and biomechanical stimulation, improving matrix reorganization and vascular maturation.

3.8. *In vivo* GelMA/C hydrogel degradation and biocompatibility

Apart from ensuring cell viability and development throughout, in vivo biocompatibility of bioink, and their degradation byproducts, is necessary for tissue development and remodeling over long-term implantation. Additionally, another major consideration is the balance between implant degradation rate and neo-tissue formation. Subcutaneous implantation was performed on C57BL/6 N mice to evaluate the biocompatibility of GelMA/C hydrogels. It is observed that the hydrogel disks slowly were degraded in vivo during the 16-week evaluation period, although complete disappearance did not occur during the experimental period (figures S9(A)-(D)). Compared to photo-crosslinked GelMA hydrogels (the hydrolysis and enzymatic cleavage of the amide bonds in the gelatin backbone), the GelMA/C showed a slower degradation due to the strong crosslinking of dopamine chemistry (figure S9(E)). The slow degradation is thought to be beneficial for structural stability of the 3D bioprinted vasculature, minimizing the risk of the walls thinning or weakening over the long-term process of vascular regeneration.

Furthermore, at different time intervals, the host tissues surrounding the hydrogel disks were collected and then stained by H&E to examine the inflammatory response. H&E is typically a pathological evaluation for the inflammatory response of implants. After the first week, only the outer margins of the hydrogel were infiltrated by immune cells, and few monocytes, indicating an acute inflammatory reaction in the initial stage (figure S9(A)). By 4 weeks, the number of infiltrating cells mildly increased, including monocytes and macrophages, and a fibrosis layer appeared around the hydrogel (figure S9(B)). By 8 weeks, the number of infiltrating inflammatory cells was dramatically reduced, as had the extent to which the material had been infiltrated through the center of the hydrogel. A fibrosis capsule was formed, and completely encircled the hydrogel (figure S9(C)). At 16 weeks post-implantation, the immune cells had almost disappeared, and only fibrosis was observed, indicating the appearance of an appreciable inflammatory response (figure S9(D)). Additionally, there was none of any obvious tissue necrosis, edema, hyperemia, hemorrhaging, and muscle damage observed during

the experimental period. Histological analysis showed the materials could be degraded slowly, and the tissue reaction *in vivo* was consistent with a typical foreign body reaction with no severe chronic inflammation, implying that the synthetic material may be suitable for *in vivo* applications.

3.9. *In vivo* vasculature development in the immunodeficient murine model

To determine whether the constructs could support implanted cell survival and functionalization, the cellladen vascular constructs were immediately implanted into NOD-SCID IL-2 receptor gamma null (NSG) mice after bioprinting. The subcutaneous tissue or hypodermis, consisting primarily of loose connective tissue and lobules of fat, contains a large number of blood vessels, suitable for the implantation of soft vascular constructs. To observe the 'fugitive-migration' behavior and implanted cell development in situ, there was neither performed the in vitro culture before implantation nor directly sutured the constructs with the host's circulation. In addition to developing engineered blood vessels, the in situ vascular development is significantly important for complex tissue regeneration.

Seeing that the hollow vasculature was easily crushed, after bioprinting the vasculature was mounted with a supporting GelMA hydrogel on the opposite side of muscle tissue), and then implanted into the dorsal region of the mice. The mount may help stabilize the vasculature in vivo, avoiding distortion from vigorous activity. It is noted that to eliminate the nonspecific reaction of cell staining, human-specific vascular markers were used, and the images were taken from the implant parts without any host tissue in the following slide examination. Figure 6(A) shows the cross-sectional schematics of a single-vessel cut from the bioprinted vascular construct, including HCASMC-laden GelMA/C hydrogel (shell) and HUVEC-laden fugitive slurry (core). At 1-week postimplantation, histological examination by H&E staining revealed that the vascular constructs were stratified in vivo and the fugitive slurry was embedded in the lumen of the vasculature (figure 6(B)). The HCASMCs and HUVECs were extruded from the shell and core layers of the axial bioprinter, respectively; therefore, HCASMCs (blue arrow) and HUVECs (red arrow) appear in the different regions of the images. Since the thin vascular wall slipped or was easily broken during the staining process, it was unable to observe the intact vascular structure in the images. Figure 6(C) shows H&E, Masson, and immunofluorescence (Hoechst, blue; CD31, red; α -SMA, green) stained images of the implanted vascular constructs with 10× cross-sectional view at week 1, 2, 4, and 6. All of these images show the same area that the cuts were performed in figures 6(A) and (B). By the second week, a bilayered vascular structure surrounded by host murine fibrosis

tissue was observed, accompanied by the gradual removal of the fugitive slurry in the lumen of the vasculature. Small vessels (red circles) containing erythrocytes emerged, and connected the host cell layer with the implanted construct. These infiltrated murine blood vessels indicated functional connections, or connections occurring between 3D bioprinted vasculature and host murine vasculature. Although there is no inflammation response for the implants in the NSG mice, the fibrosis based on the native healing mechanism could involve stimulated fibroblasts laying down connective tissue. Thus, proliferation and activation of fibroblasts deposited ECM onto the surface of 3D bioprinted vasculature for the formation of surrounding connective tissue (tunica adventitia). The artificial structure (dual layer) of the 3D bioprinted vasculature was developed to replicate a mature and biomimetic vessel with three native layers (although the tunica adventitia was formed by the migrated fibroblasts of mice). After 4 weeks, numerous small vessels (red circles) were uniformly distributed throughout the host fibrosis tissue, and implanted vascular constructs highlighted using H&E staining. Masson staining also verified host murine fibrosis (or connective tissue, blue fibers) surrounded the 3D bioprinted vasculature (muscle fibers, red fibers and pick cytoplasm). Compared to the results at 2 weeks, a compact murine fibrosis tissue occurred, and further fused, with the implanted smooth muscle layer. After 6 weeks of implantation, a typical remodeling process of the vascular structure containing distinct connective tissue layer (tunica adventitia), smooth muscle layer (tunica media), and endothelium (tunica intima) was observed. Moreover, the inset images also verified that some small capillaries existed in the 3D bioprinted vasculature, which sprouted from the host vessel of the mice. The host vessel invasion provided a beneficial microenvironment for implanted vasculature through an exchange of nutrients and oxygen. It is deduced that the host murine fibroblasts were involved in matrix reorganization, and enhanced muscularized vessel maturation in the vascular development illustrated by the Masson staining results.

Overall, these *in vivo* results uniquely demonstrated the *in vivo* development process of 3D bioprinted vasculature, including the formation of functional vessels and *in vivo* autonomous connection [33, 34]. As mentioned above, the current vascular construct is not robust enough to directly connect the blood circulation, although the *in vivo* perfusion is a perfect model for the current system. The 3D bioprinted vasculature will be further optimized in the future study to satisfy these requirements in potential clinical application. It is expected that this study will advance the success of vascular bioprinting that enables growth and maturation of thick tissues with critical defects through the support of vascularization driven by natural processes in the body.

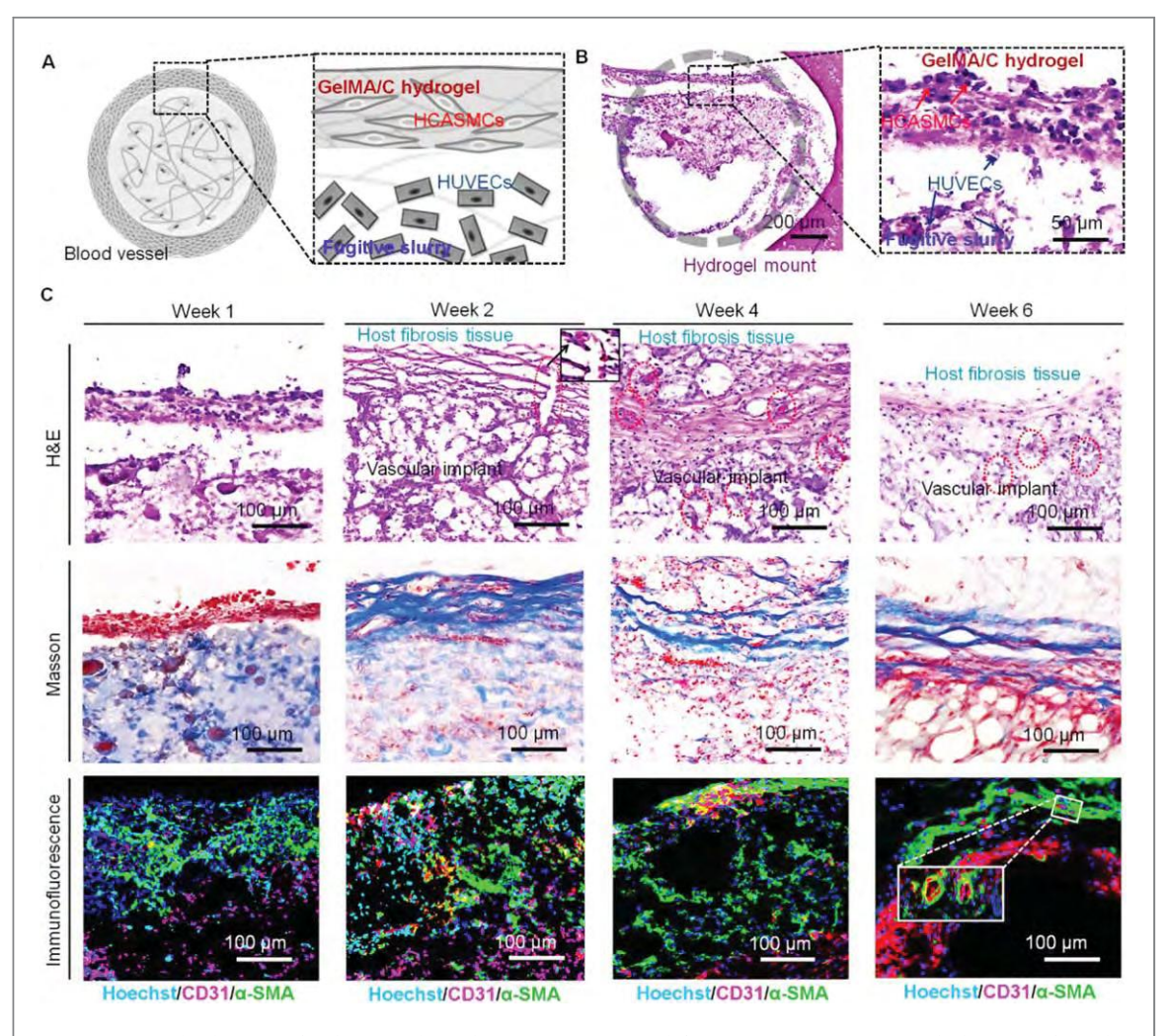


Figure 6. In vivo development of 3D bioprinted vasculature in NSG immunodeficient mice. (A) Cross-sectional schematics of a single-vessel that was cut from the bioprinted vasculature construct, including HCASMC-laden GelMA/C hydrogel (shell) and HUVEC-laden fugitive slurry (core). (B) H&E stained sections of the cell-laden vasculature with $1\times$ and $20\times$ cross-sectional view harvested at week 1. Gray circle indicates a round vessel lumen encircled by GelMA hydrogel mount. A distinct interface was observed between HCASMC-laden GelMA/C hydrogel and HUVEC-laden fugitive slurry. Some HUVECs adhered to the surface of GelMA/C hydrogel. (C) H&E, Masson, and immunofluorescence (Hoechst, blue; CD31, red; α -SMA, green) stained images of the implanted vasculature construct with 10x cross-sectional view at week 1, 2, 4, and 6. After 2 weeks of implantation, the vasculature was surrounded by the activated host fibroblasts. Vessels (red circles) containing erythrocytes connected the host cell layer with the implants highlighted with an enlarged image (black square). Masson stained images show the host murine fibrosis (or connective tissue, blue fibers) surrounding the 3D bioprinted vasculature. Immunofluorescence images show the structural feature of the vasculature constructs, which is endothelium (red) surrounded by smooth muscle (green). After 6 weeks of implantation, a hollow and mature vessel structure with compact smooth muscle and endothelium was gradually generated. The inset image shows some small vessels generated in the bioprinted vasculature construct.

4. Conclusions

In summary, a novel bioink and a manufacturing method associated with a comprehensive post-bio-printing process were developed to create vascular constructs with necessary architectures (straight and bifurcated tubular structure). The major advantage of this method over others is the 3D bioprinted vasculature replicates biomimetic vessel structures, essentially consisting of smooth muscle and endothelium, with the goal of addressing crucial challenges of a small-diameter blood vessel network. Bio-functionalization and dynamic stimuli dramatically improved vascular remodeling of both smooth muscle and endothelium. Favorable biocompatibility *in vivo* ensured the implantation safety of the material for further clinical

application. Studies of 3D bioprinted vasculature development in immunodeficient mice verified the effectiveness of the design. Although more optimization is required to improve the bioprinted vascular construct, advanced achievements in creating biomimetic, functional vasculature show significant potential toward eventually fabricating a complicated tissue/organ for clinical transplantation.

Acknowledgments

This work is supported by NIH Director's New Innovator Award 1DP2EB020549-01 and NSF BMMB program grant # 1854415. The authors would like to thank Dr Nathan Castro, Ryan Herbst, and Allison

Below for help on the bioprinter design and fabrication.

Author contributions

HC and LGZ conceived the ideas and designed the experiments. HC, WZ, YC, SL, and XZ conducted the experiments. HC, MN, and SM performed data analysis. YH, CL, ZY, YZ, SW, MM, and KH designed and carried out animal experiments. HC, MN, SM, and LGZ prepared the manuscript.

Competing financial interests

The authors declare no competing financial interests.

Data availability

The authors declare that all data supporting the findings of this study are available within the paper and its supplementary information, source data for the figures in this study are available from the authors upon request.

ORCID iDs

References

- [1] Forgacs G 2012 Tissue engineering: perfusable vascular networks *Nat. Mater.* 11 746–7
- [2] Novosel E C, Kleinhans C and Kluger P J 2011 Vascularization is the key challenge in tissue engineering Adv. Drug Deliv. Rev. 63 300–11
- [3] Rouwkema J and Khademhosseini A 2016 Vascularization and angiogenesis in tissue engineering: beyond creating static networks *Trends Biotechnol.* 34 733–45
- [4] Cui H, Miao S, Esworthy T, Zhou X, Lee S J, Liu C, Yu Z X, Fisher J P, Mohiuddin M and Zhang L G 2018 3d bioprinting for cardiovascular regeneration and pharmacology Adv. Drug Deliv. Rev. 132 252–69
- [5] Cui H, Nowicki M, Fisher J P and Zhang L G 2017 3d bioprinting for organ regeneration Adv. Healthcare Mater. 6 1601118
- [6] Cui H, Zhu W, Nowicki M, Zhou X, Khademhosseini A and Zhang L G 2016 Hierarchical fabrication of engineered vascularized bone biphasic constructs via dual 3d bioprinting: integrating regional bioactive factors into architectural design Adv. Healthcare Mater. 5 2174–81
- [7] Rouwkema J, Rivron N C and van Blitterswijk C A 2008 Vascularization in tissue engineering *Trends Biotechnol.* 26 434–41
- [8] Seifu D G, Purnama A, Mequanint K and Mantovani D 2013 Small-diameter vascular tissue engineering Nat. Rev. Cardiol. 10 410–21
- [9] Gui L and Niklason L E 2014 Vascular tissue engineering: building perfusable vasculature for implantation *Curr. Opin. Chem. Eng.* 3 68–74

- [10] Bersini S and Moretti M 2015 3D functional and perfusable microvascular networks for organotypic microfluidic models J. Mater. Sci., Mater. Med. 26 180
- [11] Nemeno-Guanzon J G, Lee S, Berg J R, Jo Y H, Yeo J E, Nam B M, Koh Y G and Lee J I 2012 Trends in tissue engineering for blood vessels J. Biomed. Biotechnol. 2012 956345
- [12] Hasan A, Paul A, Vrana N E, Zhao X, Memic A, Hwang Y S, Dokmeci M R and Khademhosseini A 2014 Microfluidic techniques for development of 3d vascularized tissue *Biomaterials* 35 7308–25
- [13] Kolesky D B, Homan K A, Skylar-Scott M A and Lewis J A 2016 Three-dimensional bioprinting of thick vascularized tissues Proc. Natl Acad. Sci. USA 113 3179–84
- [14] Zhang B et al 2016 Biodegradable scaffold with built-in vasculature for organ-on-a-chip engineering and direct surgical anastomosis Nat. Mater. 15 669–78
- [15] Miller J S et al 2012 Rapid casting of patterned vascular networks for perfusable engineered three-dimensional tissues Nat. Mater. 11 768–74
- [16] Kolesky D B, Truby R L, Gladman A S, Busbee T A, Homan K A and Lewis J A 2014 3d bioprinting of vascularized, heterogeneous cell-laden tissue constructs Adv. Mater. 26 3124–30
- [17] Mirabella T, MacArthur J W, Cheng D, Ozaki C K, Woo Y J, Yang M T and Chen C S 2017 3d-printed vascular networks direct therapeutic angiogenesis in ischaemia *Nat. Biomed. Eng.* 1 0083
- [18] Hann S Y, Cui H, Esworthy T, Miao S, Zhou X, Lee S J, Fisher J P and Zhang L G 2019 Recent advances in 3d printing: vascular network for tissue and organ regeneration *Transl. Res.* 211 46–63
- [19] Elliott M B and Gerecht S 2016 Three-dimensional culture of small-diameter vascular grafts J. Mater. Chem. B 4 3443–53
- [20] Haga J H, Li Y S and Chien S 2007 Molecular basis of the effects of mechanical stretch on vascular smooth muscle cells J. Biomech. 40 947–60
- [21] Li Y S, Haga J H and Chien S 2005 Molecular basis of the effects of shear stress on vascular endothelial cells J. Biomech. 38 1949–71
- [22] Lehoux S and Tedgui A 2003 Cellular mechanics and gene expression in blood vessels J. Biomech. 36 631–43
- [23] Lesman A, Rosenfeld D, Landau S and Levenberg S 2016 Mechanical regulation of vascular network formation in engineered matrices Adv. Drug Deliv. Rev. 96 176–82
- [24] Huang A H and Niklason L E 2014 Engineering of arteries in vitro Cell. Mol. Life Sci. 71 2103–18
- [25] Chistiakov D A, Orekhov A N and Bobryshev Y V 2017 Effects of shear stress on endothelial cells: go with the flow Acta Physiol. 219 382–408
- [26] Chiu J J and Chien S 2011 Effects of disturbed flow on vascular endothelium: pathophysiological basis and clinical perspectives *Physiol. Rev.* 91 327–87
- [27] CHLUPÁČ E F J and Bačáková L 2009 Blood vessel replacement: 50 years of development and tissue engineering paradigms in vascular surgery *Physiol. Res.* 58 S119–39
- [28] Ryu J H, Lee Y, Kong W H, Kim T G, Park T G and Lee H 2011 Catechol-functionalized chitosan/pluronic hydrogels for tissue adhesives and hemostatic materials *Biomacromolecules* 12 2653–9
- [29] Kim S H, Lee S H, Lee J E, Park S J, Kim K, Kim I S, Lee Y S, Hwang N S and Kim B G 2018 Tissue adhesive, rapid forming, and sprayable ecm hydrogel via recombinant tyrosinase crosslinking *Biomaterials* 178 401–12
- [30] Davies P F 2009 Hemodynamic shear stress and the endothelium in cardiovascular pathophysiology Nat. Clin. Pract. Cardiovasc. Med. 6 16–26
- [31] Lee V K, Kim D Y, Ngo H, Lee Y, Seo L, Yoo S S, Vincent P A and Dai G 2014 Creating perfused functional vascular channels using 3d bio-printing technology *Biomaterials* 35 8092–102
- [32] Loessner D, Meinert C, Kaemmerer E, Martine L C, Yue K, Levett P A, Klein T J, Melchels F P, Khademhosseini A and

- Hutmacher D W 2016 Functionalization, preparation and use of cell-laden gelatin methacryloyl-based hydrogels as modular tissue culture platforms *Nat. Protocols* 11 727–46
- [33] Koshy S T, Ferrante T C, Lewin S A and Mooney D J 2014 Injectable, porous, and cell-responsive gelatin cryogels *Biomaterials* 35 2477–87
- [34] Cui H, Zhu W, Holmes B and Zhang L G 2016 Biologically inspired smart release system based on 3d bioprinted perfused scaffold for vascularized tissue regeneration Adv. Sci. 3 1600058
- [35] Hong S, Yang K, Kang B, Lee C, Song IT, Byun E, Park K I, Cho S W and Lee H 2013 Hyaluronic acid catechol: a biopolymer exhibiting a ph-dependent adhesive or cohesive property for human neural stem cell engineering Adv. Funct. Mater. 23 1774–80
- [36] Li L, Yan B, Yang J, Chen L and Zeng H 2015 Novel musselinspired injectable self-healing hydrogel with anti-biofouling property Adv. Mater. 27 1294–9
- [37] Liu Y, Ai K and Lu L 2014 Polydopamine and its derivative materials: synthesis and promising applications in energy, environmental, and biomedical fields *Chem. Rev.* 114 5057–115
- [38] Shin M et al 2017 Complete prevention of blood loss with self-sealing haemostatic needles Nat. Mater. 16 147–52
- [39] Lee B P, Dalsin J L and Messersmith P B 2002 Synthesis and gelation of dopa-modified poly(ethylene glycol) hydrogels *Biomacromolecules* 3 1038–47
- [40] Park H J, Jin Y, Shin J, Yang K, Lee C, Yang H S and Cho S W 2016 Catechol-functionalized hyaluronic acid hydrogels enhance angiogenesis and osteogenesis of human adipose-derived stem cells in critical tissue defects *Biomacromolecules* 17 1939–48
- [41] Chen Y C, Lin R Z, Qi H, Yang Y, Bae H, Melero-Martin J M and Khademhosseini A 2012 Functional human vascular network generated in photocrosslinkable gelatin methacrylate hydrogels Adv. Funct. Mater. 22 2027–39
- [42] Shin J et al 2015 Tissue adhesive catechol-modified hyaluronic acid hydrogel for effective, minimally invasive cell therapy Adv. Funct. Mater. 25 3814–24
- [43] Gao G et al 2017 Tissue engineered bio-blood-vessels constructed using a tissue-specific bioink and 3d coaxial cell printing technique: a novel therapy for ischemic disease Adv. Funct. Mater. 27 1700798
- [44] Colosi C, Shin S R, Manoharan V, Massa S, Costantini M, Barbetta A, Dokmeci M R, Dentini M and Khademhosseini A 2016 Microfluidic bioprinting of heterogeneous 3d tissue constructs using low-viscosity bioink Adv. Mater. 28 677–84
- [45] Gao Q et al 2017 3d bioprinting of vessel-like structures with multilevel fluidic channels ACS Biomater. Sci. Eng. 3 399–408
- [46] Jia W et al 2016 Direct 3d bioprinting of perfusable vascular constructs using a blend bioink *Biomaterials* 106 58–68
- [47] Gao Q, He Y, Fu J Z, Liu A and Ma L 2015 Coaxial nozzleassisted 3d bioprinting with built-in microchannels for nutrients delivery *Biomaterials* 61 203–15
- [48] Ozbolat I T and Hospodiuk M 2016 Current advances and future perspectives in extrusion-based bioprinting *Biomaterials* 76 321–43
- [49] Lee K Y and Mooney D J 2012 Alginate: properties and biomedical applications Prog. Polym. Sci. 37 106–26
- [50] Pratt K J, Jarrell B E, Williams S K, Carabasi R A, Rupnick M A and Hubbard F A 1988 Kinetics of endothelial cell—surface attachment forces J. Vasc. Surg. 7 591–9
- [51] Reinhart-King C A 2008 Endothelial cell adhesion and migration *Methods Enzymol*. vol 443 (New York: Academic) pp 45–64

- [52] Dalaty A A, Karam A, Najlah M, Alany R G and Khoder M 2016 Effect of non-cross-linked calcium on characteristics, swelling behaviour, drug release and mucoadhesiveness of calcium alginate beads Carbohydrate Polym. 140 163–70
- [53] Bajpai S K and Sharma S 2004 Investigation of swelling/ degradation behaviour of alginate beads crosslinked with Ca²⁺ and Ba²⁺ ions React. Funct. Polym. 59 129–40
- [54] Zhu W, Castro N J, Cui H, Zhou X, Boualam B, McGrane R, Glazer R I and Zhang L G 2016 A 3d printed nano bone matrix for characterization of breast cancer cell and osteoblast interactions *Nanotechnology* 27 315103
- [55] Miao S, Zhu W, Castro N J, Nowicki M, Zhou X, Cui H, Fisher J P and Zhang L G 2016 4d printing smart biomedical scaffolds with novel soybean oil epoxidized acrylate Sci. Rep. 6 27226
- [56] Zhou X, Cui H, Nowicki M, Miao S, Lee S J, Masood F, Harris B T and Zhang L G 2018 Three-dimensional-bioprinted dopamine-based matrix for promoting neural regeneration ACS Appl. Mater. Interfaces 10 8993–9001
- [57] Peattie R A, Rieke E R, Hewett E M, Fisher R J, Shu X Z and Prestwich G D 2006 Dual growth factor-induced angiogenesis in vivo using hyaluronan hydrogel implants Biomaterials 27 1868–75
- [58] Webbera M J, Tongersb J, Losordob D W, Newcombd C J and Stuppd S I 2011 Supramolecular nanostructures that mimic vegf as a strategy for ischemic tissue repair *Proc. Natl Acad. Sci.* USA 108 13438–43
- [59] Sukriti S, Tauseef M, Yazbeck P and Mehta D 2014 Mechanisms regulating endothelial permeability Pulm. Circ. 4 535–51
- [60] Russo G, Leopold J A and Loscalzo J 2002 Vasoactive substances: nitric oxide and endothelial dysfunction in atherosclerosis Vasc. Pharmacol. 38 259–69
- [61] Allen B W, Stamler J S and Piantadosi C A 2009 Hemoglobin, nitric oxide and molecular mechanisms of hypoxic vasodilation *Trends Mol. Med.* 15 452–60
- [62] Casino P R, Kilcoyne C M, Quyyumi A A, Hoeg J M and Panza J A 1993 The role of nitric oxide in endotheliumdependent vasodilation of hypercholesterolemic patients Circulation 88 2541–7
- [63] Fernandez C E, Yen R W, Perez S M, Bedell H W, Povsic T J, Reichert W M and Truskey G A 2016 Human vascular microphysiological system for *in vitro* drug screening *Sci. Rep.* 6 21579
- [64] Amento E P, Ehsani N, Palmer H and Libby P 1991 Cytokines and growth factors positively and negatively regulate interstitial collagen gene expression in human vascular smooth muscle cells Arterioscler. Thromb. 11 1223–30
- [65] Schlumberger W, Thie M, Rauterberg J and Robenek H 1991 Collagen synthesis in cultured aortic smooth muscle cells. Modulation by collagen lattice culture, transforming growth factor-beta 1, and epidermal growth factor Arterioscler. Thromb. 11 1660–6
- [66] Syedain Z H, Meier L A, Bjork J W, Lee A and Tranquillo R T 2011 Implantable arterial grafts from human fibroblasts and fibrin using a multi-graft pulsed flow-stretch bioreactor with noninvasive strength monitoring *Biomaterials* 32 714–22
- [67] Weidenhamer N K and Tranquillo R T 2013 Influence of cyclic mechanical stretch and tissue constraints on cellular and collagen alignment in fibroblast-derived cell sheets *Tissue Eng.* C 19 386–95
- [68] Malek A M, Alper S L and Izumo S 1999 Hemodynamic shear stress and its role in atherosclerosis J. Am. Med. Assoc. 282 2035–42